

Characteristics of Dust Storms Generated by Trapped Waves in the Lee of Mountains

Amato T. Evan^a William C. Porter^b Rachel Clemesha^a Alex Kuwano^a and Robert Frouin^a

^a *Scripps Institution of Oceanography, University of California San Diego*

^b *Department of Environmental Sciences, University of California Riverside*

This manuscript is in review at Journal of the Atmospheric Sciences

Corresponding author: Amato Evan, aevan@ucsd.edu

7 ABSTRACT: In-situ observations and output from a numerical model are utilized to examine
8 three dust outbreaks that occurred in the northwestern Sonoran Desert. Via analysis of these
9 events it is shown that trapped waves generated in the lee of an upwind mountain range produced
10 high surface wind speeds along the desert floor and the observed dust storms. Based on analysis
11 of observational and model output general characteristics of dust outbreaks generated by trapped
12 waves are suggested, including dust layer depths and concentrations that are dependent upon wave
13 phase and height above the surface, emission and transport associated with the presence of a low-
14 level jet, and wave-generated high wind speeds and thus emission that occurs far downwind of the
15 wave source. Trapped lee waves are ubiquitous in the Earth's atmosphere and thus it is likely that
16 the meteorological aspects of the dust storms examined here are also relevant to understanding dust
17 in other regions. These dust outbreaks occurred near the Salton Sea, an endorheic inland body of
18 water that is rapidly drying due to changes in water use management. As such, these findings are
19 also relevant in terms of understanding how future changes in size of the Salton Sea will impact
20 dust storms and air quality there.

21 SIGNIFICANCE STATEMENT: Dust storms are ubiquitous in the Earth’s atmosphere, yet the
22 physical processes underlying dust emission and subsequent transport are not always understood,
23 in-part due to the wide variety of meteorological processes that can generate high winds and dust.
24 Here we use in-situ measurements and numerical modeling to demonstrate that vertically trapped
25 atmospheric waves generated by air flowing over a mountain are one such mechanism that can
26 produce dust storms. We suggest several features of these dust outbreaks that are specific to their
27 production by trapped waves. As the study area is a region undergoing rapid environmental change,
28 these results are relevant in terms of predicting future dust there.

29 **1. Introduction**

30 Aeolian dust is one of the most pervasive aerosols in the Earth’s atmosphere (Huneeus et al.
31 2011). Dust alters the planet’s radiative budget and hydrological cycles via aerosol direct and
32 indirect effects (Choobari et al. 2014) and affects nutrient cycling in the marine and terrestrial
33 ecosystems where dust emission and deposition occurs (Field et al. 2010). As such, there is a need
34 to understand how planetary climate change has—and will continue to—influence the processes of
35 dust emission, transport, and deposition, the so-called dust cycle (Shao et al. 2011), as well as
36 to understand how those forced changes in the dust-cycle feedback onto the Earth’s climate (Kok
37 et al. 2018). However, studies examining the representation of dust in model output from the fifth
38 and sixth Climate Model Intercomparison Projects have identified model biases in the dust mean
39 state, poor reproduction of historical dust variability, and insufficient sensitivity of dust emission
40 to changes in surface conditions (Pu and Ginoux 2018; Zhao et al. 2022), casting doubt on our
41 ability to model future dust.

42 Improving understanding of the physical processes leading to dust emission and transport can lead
43 to advances in the representation of dust in models. Although there is a growing body of knowledge
44 of the meteorological processes underlying dust storms (Knippertz 2014), there remains a dearth
45 of representative in-situ observations in dust emitting regions, which is not entirely surprising
46 given that most dust outbreaks occur in sparsely populated regions (Prospero et al. 2002) where
47 challenges associated with access can be significant (e.g., Giles 2005). This study aims to add to
48 understanding of the meteorological processes affecting dust storms by examining measurements
49 made during three dust outbreaks in a region of southeastern California, with a specific focus

50 on the role of complex terrain in shaping the characteristics of the high winds and lofted dust.
51 Previous studies have identified several processes associated with orographically-forced flow that
52 result in high winds and dust lofting, including gap flow (Evan et al. 2016; Jiang et al. 2009; Todd
53 et al. 2008), downslope winds due to orographic precipitation and latent cooling of air (Knippertz
54 et al. 2007; Evan et al. 2022c), generic Foehn events (Gläser et al. 2012; Evan 2019), and lee-side
55 rotor circulations (Grubišić and Billings 2007; Pokharel et al. 2017). Here we focus on the role of
56 trapped lee-waves in generating dust outbreaks.

57 Trapped lee waves are a class of orographically forced waves (i.e., generated by air flowing over a
58 mountain range) for which the waves are trapped in the lower atmosphere, rather than propagating
59 upwards through the troposphere (Nappo 2013), propagating laterally well beyond the location of
60 wave generation (Durran 2003). Vertical variations in stability and shear in the upstream flow (i.e.,
61 upwind of the mountain range) give rise to trapped waves (Scorer 1949), and temporal changes in
62 these properties result in non-stationary waves (Ralph et al. 1997). Trapped waves can give rise
63 to rotors in the downslope flow, in which rapid vertical ascent in the upward branch of a wave can
64 produce flow separation at the surface and reversed surface winds under the wave crest (Doyle and
65 Durran 2002), and modify (both accelerate and decelerate) surface wind speeds far beyond the
66 wave source (Durran 1986).

67 While there is a rich history of scholarly work on the topic of trapped lee waves (c.f., Smith
68 2019), to the best of our knowledge studies connecting trapped waves to dust emission and transport
69 have been limited to the Owen’s Valley, and more strongly focused on the dynamics of the lee-side
70 circulation than the characteristics of the subsequent dust storms (Grubišić et al. 2008; De Wekker
71 and Mayor 2009; Jiang et al. 2011; Strauss et al. 2016). Additionally, Owen’s Valley is narrow and
72 consequently waves forming in the lee of the Eastern Sierra are distinct from trapped lee waves that
73 are able to propagate long distances downwind of the region of wave generation. Given the ubiquity
74 of trapped lee waves in the Earth’s atmosphere it is at least plausible that these orographically forced
75 phenomena are responsible for a non-negligible fraction of the global dust uplift (e.g., downwind
76 of the Atlas or Andes mountains).

77 Our area of interest is the Salton Basin, a sub-sea level terminal basin located at the northwestern
78 corner of the Sonoran Desert that is part of the greater Salton Trough, a northwest-southeast
79 oriented rift valley along the San Andreas Fault (Fig. 1). At the lowest elevations of the basin lies

80 the Salton Sea, an endorheic body of water having an average surface height of -72.7 m AMSL
81 in 2021 (dashboard.waterdata.usgs.gov accessed on March 24, 2022). Dust storms are a
82 frequent occurrence in this region (Evan 2019), which is due in part to the prevalence of erodible
83 soils (Buck et al. 2011; Sweeney et al. 2011). The Salton Sea was accidentally created in 1905
84 during an attempt to irrigate the southern portion of the Salton Trough (the Imperial Valley), but
85 more recently the volume of the Sea has been declining due to a 2003 water transfer agreement
86 that resulted in diversion of water from the Sea. Consequently, the size of the Salton Sea is rapidly
87 declining (Poudel et al. 2021).

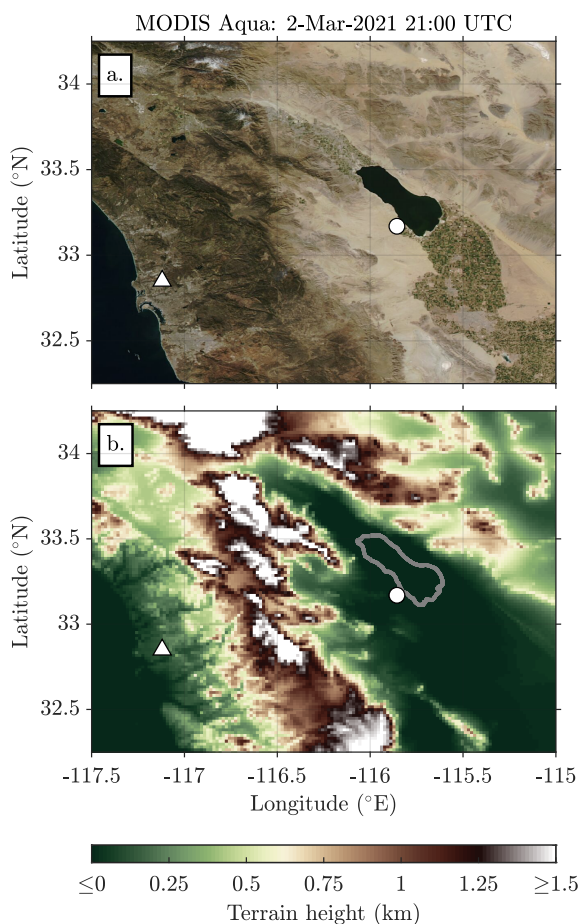
88 Playa sources represent a significant fraction of all dust emission associated with human activity
89 (Ginoux et al. 2012), and the drying of bodies of water in arid regions increases the incidence and
90 intensity of dust storms there (Zucca et al. 2021). A simulation of a single dust event in the Salton
91 Basin estimated an approximately 10% increase in dust burden with a nearly 40% growth in the
92 playa surface (Parajuli and Zender 2018), which is significant given that the playa is surrounded
93 by desert dust sources that are vastly larger in spatial extent. Other work has shown adverse health
94 effects from exposure to dust emitted from the playa (Burr et al. 2021; Biddle et al. 2021), which
95 contains anthropogenic trace metals (Frie et al. 2019). As such, improving understanding of the
96 meteorology underlying dust events in this region is useful in terms of understanding the changing
97 dust burden and the associated human health impacts.

98 The remainder of this article is organized as follows. In Section 2 we describe the observational
99 data and model output used in the study. In Section 3 we examine the meteorological and physical
100 aspects of three dust storms via measurements and model output. In Section 4 we discuss general
101 characteristics of dust storms generated by trapped lee waves. In Section 5 we summarize the work
102 presented here, note the broader implications of the findings, and suggest additional observations
103 and modeling studies to address remaining questions.

104 **2. Observations and Model**

105 We start by describing the region of interest (Fig. 1). The Salton Basin is an arid endorheic
106 basin that typically receives less than 100 mm of precipitation each year (Stephen and Gorsline
107 1975; NCEI). The morphology of the area includes alluvial fans, sand and sand dunes, dry washes,
108 paleo lakebed, and rock and vegetated surfaces (IID 2016). Within the basin, the Salton Sea is a

109 spatially large yet shallow inland body of water. Agriculture land is found immediately to the north
110 and south of the Salton Sea, whereas the Anza desert, from which many dust storms in the area
111 originate, lies immediately to its west (Fig. 1a). The Basin is bounded to the west by the Peninsular
112 Range, to the north by the San Bernardino Mountains, and to the east by the Transverse Range,
113 while the topography gradually slopes upward to the south before dropping into the Colorado River
114 Delta (Fig. 1b).



115 FIG. 1. Terrain of the region of interest. Shown in 1a is a true color image acquired from MODIS-Aqua on
116 March 2, 2021 at 21:00 UTC. Shown in 1b is an elevation map of the same region. The approximate shoreline
117 of the Salton Sea during March 2021 is indicated by the gray contour. The locations of the field and the NKX
118 radiosonde sites are indicated by the white circles and triangles, respectively, in both panels. The desert that lies
119 immediately west of the field site is the source region for the airborne dust measured at the site.

120 *a. Field site and in-situ Observations*

121 Much of the observational data presented here was collected from a field site located near the
122 current western coastline of the Salton Sea, at approximately 33.2 N and -115.9 E (Fig. 1). The
123 site is adjacent to a large citrus and date palm farm, which provides physical security for the station
124 and allows for access to a stable source of power for instrumentation and telemetry. The landscape
125 immediately surrounding the site is characterized by narrow dry washes and cobbles distributed
126 over silt-dominated paleo lakebed with sparse shrub vegetation.

127 An AERONET CIMEL Electronique SunÅšsky photometer is located at the site, which is used
128 to measure Sun collimated direct beam irradiance and directional sky radiance at 8 spectral bands
129 centered on 1020, 870, 675, 440, 936, 500, 380, and 340 nm (Holben et al. 1998). The instrument
130 base is mounted approximately 2 m above ground level. Direct solar irradiance measurements
131 are made at 5-minute intervals. Here we utilize data from the AERONET Level 1.5 products
132 processed by the Version 3 AERONET algorithm, which provides fully automatic cloud screening
133 and instrument anomaly quality controls in near-real-time (Giles et al. 2019). We include dusty
134 observations that were erroneously classified as cloud-contaminated using the restoring algorithm
135 described in Evan et al. (2022a).

136 Located at the field site is a Vaisala CL51 ceilometer, which is a single lens lidar system that makes
137 continuous profiles of attenuated backscatter at a nominal wavelength of 910 nm and up to heights
138 of 15 km. The CL51 range corrected backscatter profiles used here are generated at a 36 s temporal
139 resolution and a 10 m vertical resolution. In addition to cloud detection, ceilometers, including the
140 CL51, have shown to be useful in the detection of aerosol layers in the lower troposphere (Münkel
141 et al. 2007; Wiegner et al. 2014; Jin et al. 2015; Marcos et al. 2018; Yang et al. 2020). The Vaisala
142 processing software for the CL51 measurements, BLView, produces retrievals of vertical profiles of
143 extinction σ and optical depth τ from the backscatter profiles for the clear-sky atmosphere below 5
144 km. Although details regarding the retrieval process used in BLView are not publicly available, we
145 are able to approximately reproduce the extinction profile retrievals using the methods described
146 in (Fernald 1984), as discussed in Evan et al. (2022c). We calibrate the 910 nm aerosol optical
147 depth (AOD) retrieved from the CL51, which is obtained by integrating the retrieved extinction
148 profiles in the vertical dimension to an equivalent 500 nm value by comparing values of 500 nm

149 AOD from AERONET to the 910 nm AOD retrieved from the CL51, following the methods in
150 Evan et al. (2022a).

151 At this site also sits a cabled Vantage Pro2 Davis Met Station, which has a suite of sensors
152 including temperature and humidity sensors under a passive radiation shield, a wind anemometer,
153 a barometer, and rainfall measurements. Data are logged at a 1-min interval. The site anemometer
154 sits approximately 2-m above ground level. The 2-m wind speed and gust measurements were
155 calibrated to an equivalent 10-m wind speed value by multiplying the 2-m values by a factor of
156 1.37, which was empirically derived via comparison to an adjacent 10-m mounted anemometer
157 (Evan et al. 2022a). We note that at present only hourly averaged values are available from the 10-m
158 anemometer, which is managed by the local water and power utility, Imperial Irrigation District.

159 Vertical profiles of temperature, humidity, pressure and wind are obtained from Vaisala RS-41
160 sondes launched at the site on March 9, 2021 (at 1203, 1505, 1803, 1934, 2102, 2234, and 2359
161 UTC), March 15, 2021 (at 2114 and 2320 UTC), and February 15, 2022 (at 2105, 2242, and 2340
162 UTC). Lastly, all heights from soundings and the CL51 are referenced to ground level of the station,
163 which sits approximately 32 m below mean sea level. Radiosonde, meteorological station, and
164 ceilometer profiles made at the field site are permanently archived and publicly available (Evan
165 et al. 2022b).

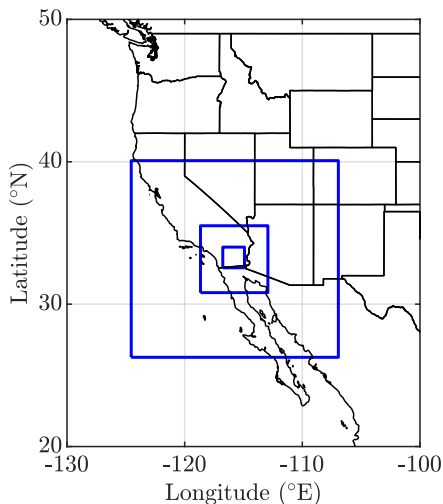
166 *b. Other Data*

167 In addition to the measurements made at the field site we utilize surface meteorological and
168 PM₁₀ measurements made from stations around the Salton Sea. The meteorological and PM₁₀
169 data were accessed via the MesoWest network (Horel et al. 2002) and the California Air Resources
170 Board Air Quality and Meteorological Information System. We also utilize imagery from a 360°
171 Roundshot web camera that is located 28 km west of the field site at an elevation of 300 m AGL,
172 which are available at approximately 10 min intervals during daytime hours. We incorporate
173 into our analysis satellite imagery from the Moderate Resolution Imaging Spectrometer (MODIS)
174 flying onboard the Aqua satellite, which were generated from the NASA Earth Observing System
175 Data and Information System (EOSDIS) Worldview application. We also generated imagery from
176 radiance measurements made by the Advanced Baseline Imager (ABI) flying onboard GOES-17.
177 These data were accessed from the NOAA Comprehensive Large Array-data Stewardship System.

178 We examine measurements collected from radiosondes launched from the NKX sounding station,
179 which is near the coastline (white triangle, Fig. 1), where radiosondes are launched twice daily at
180 00:00 and 24:00 UTC. Three-hourly output from the North American Regional Reanalysis (NARR),
181 which is provided on 29 vertical layers at a 32-km horizontal resolution, is used to examine the
182 synoptic environment associated with the dust outbreaks studied here (Mesinger et al. 2006).

183 *c. WRF Model*

184 Numerical simulations of the meteorology underlying the dust cases examined here were made
185 using the Advanced Research version of the Weather Research and Forecasting (WRF) Model
186 (Skamarock et al. 2019) version 4.3. The model was run using 3-domain, nested 2-way interactive
187 grid with horizontal resolutions of 15, 5, and 1 km (Fig. 2). The model was initialized using data
188 from the Global Forecast System (GFS) output (NCEP 2013) at 06:00 UTC on March 8 2021,
189 March 14 2022, and February 14 2022, and was integrated forward for the subsequent 72 hours
190 for each case with the lateral boundaries of the outermost domain continuously forced by the GFS
191 output. WRF model output shown here is from the innermost domain.



192 FIG. 2. Domains for the nested WRF simulations. Plotted in blue are the horizontal extents of the nested
193 domains utilized in the WRF simulations. The horizontal resolutions of the outermost to innermost domains are
194 15, 5, and 1 km, respectively.

TABLE 1. Physics schemes employed in the WRF simulations

Parameterization	Scheme
Planetary boundary layer	Mellor–Yamada–Janjić (Janjić 1994; Janić 2001)
Surface layer	Monin-Obukhov with Janjić Eta (Monin and Obukhov 1954; Janić 2001)
Land surface physics	Noah Land Surface Model (Chen and Dudhia 2001)
Longwave & shortwave radiation	RRTMG & RRTMG (Iacono et al. 2008)
Purdue Lin scheme	(Chen and Sun 2002)
Cumulus scheme (5 & 15 km domains)	Grell3D (Grell 1993; Grell and Dévényi 2002)

195 The model top is at 10 hPa and 51 sigma vertical levels are employed, with the highest vertical
 196 resolution found in the lower troposphere. Approximately 7 half-sigma levels are found in the
 197 lowest kilometer AGL, with the first level at a height of 27 m AGL. The output shown here is
 198 from simulations using the Mellor–Yamada–Janjić (Janjić 1994) planetary boundary layer
 199 scheme, which, when compared to other boundary layer schemes, was found to best reproduce
 200 in-situ observations, particularly the surface wind speeds, in the region (Evan et al. 2022c). The
 201 model physics parameterizations used in this study are shown in Table 1. Comparisons of WRF
 202 output to surface wind measurements at the field site and radiosondes launched during the dust
 203 outbreaks considered here can be found in Supplemental Figures S1–S13.

204 We also conduct simulations using the WRF-Chem model (Grell et al. 2005; Fast et al. 2006;
 205 Peckham et al. 1991), employing the GOCART aerosol scheme without ozone chemistry (Chin
 206 et al. 2000; Ginoux et al. 2001) and the Air Force Weather Agency dust emission scheme (AFWA
 207 LeGrand et al. 2019), with other model parameterizations, setup, and forcing identical to that
 208 described for the WRF simulations (Table 1). The AFWA emissions scheme, which uses a modified
 209 version of the saltation-based dust emission function of Marticorena and Bergametti (1995), is
 210 one of several available by default in current versions of WRF-Chem. This scheme represents
 211 an update to the earlier GOCART-WRF emissions scheme, incorporating separately modeled
 212 saltation processes driving subsequent dust emissions rather than the single-step parameterization
 213 used previously. Since its addition to WRF-Chem, the AFWA scheme has been used and evaluated
 214 in dust modeling research and case studies around the world (e.g. Yuan et al. 2019; Kim et al. 2021;
 215 Miller et al. 2021). In the model dust in the size range of 0.2–20 μm is simulated in 5 bins.

216 When comparing the model simulated dust to aerosol measurements at the field site and surface
 217 PM_{10} measurements at a number of locations around the Salton Sea we found that the model

218 produced too much dust at weak wind speeds and too small an increase in dust as the wind
219 speed increased. We also found via comparison to surface PM_{10} measurements that dust surface
220 concentrations were biased low in the region of the research site, and biased high to the north and
221 south of the site (not shown). These biases persisted across two different soil erodibility input
222 maps, including the default GOCART topographic erodibility dataset of Ginoux et al. (2001), as
223 well as the more recent data set of Parajuli and Zender (2017). Based on their consistency across
224 erodibility map inputs, we suspect that these biases are related to other surface property inputs,
225 such as soil and land surface cover type.

226 Due to concerns over the representation of dust emission in the model we only utilize output
227 from a WRF-Chem simulation of the dust outbreak on March 15, 2021 in order to examine the
228 general relationship between trapped lee wave phase and the vertical and horizontal distribution of
229 dust (Section 4). We leave improvement of the representation of modeled dust in this region for
230 future work.

231 *d. Salton Sea Extent*

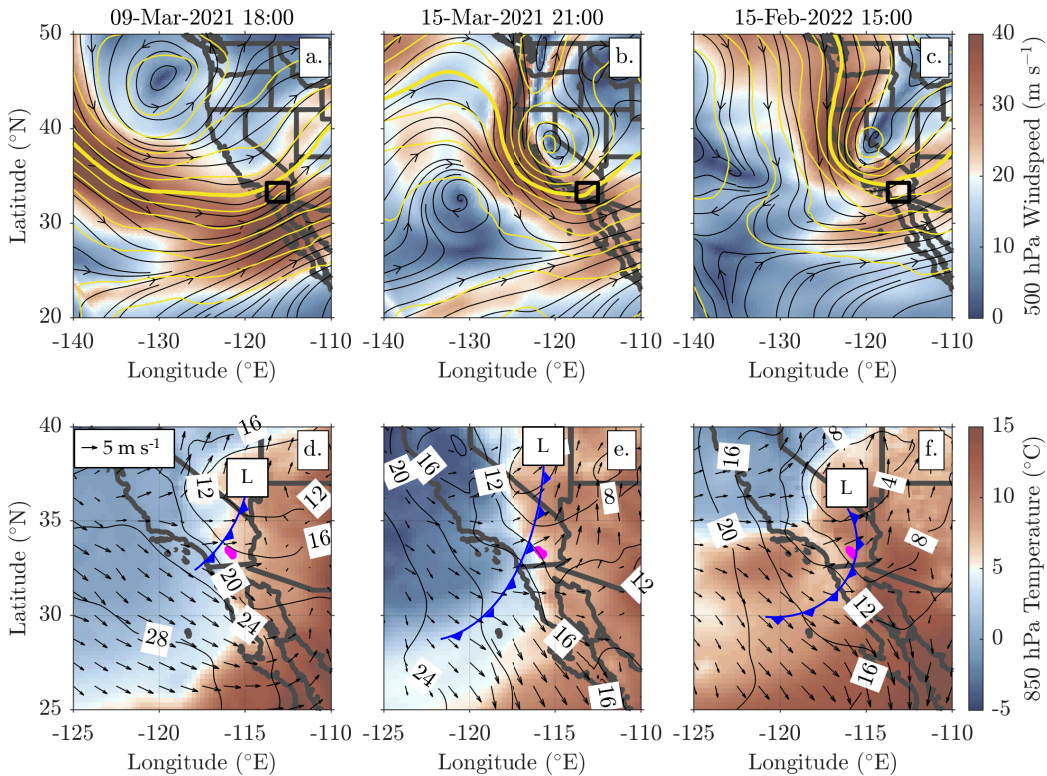
232 The extent of the Salton Sea was estimated using MODIS Aqua visible satellite imagery from
233 March 2, 2021 (Fig. 1a). To estimate the shoreline we applied an arbitrary threshold to the
234 reflectances of each of the three image color channels (i.e., red, green, blue) in order to distinguish
235 the dark Salton Sea against the bright desert surface, manually excluding any pixels that were dark
236 enough to pass this threshold test from the vegetated croplands to the south of the sea. We then
237 used these data to define the shoreline of the sea (gray contour, Fig. 1b). The shoreline estimate is
238 used as a visual aid in several figures found throughout this manuscript.

239 **3. Characteristics of the Dust Storms**

240 Here we consider three dust outbreaks within the Salton Basin: March 9 and 15, 2021, and
241 February 15, 2022. When convenient we only refer to these cases using their respective months
242 and days. These events were chosen because of the similarities in their meteorological aspects and
243 dust characteristics, and the availability of radiosonde measurements made at the field site.

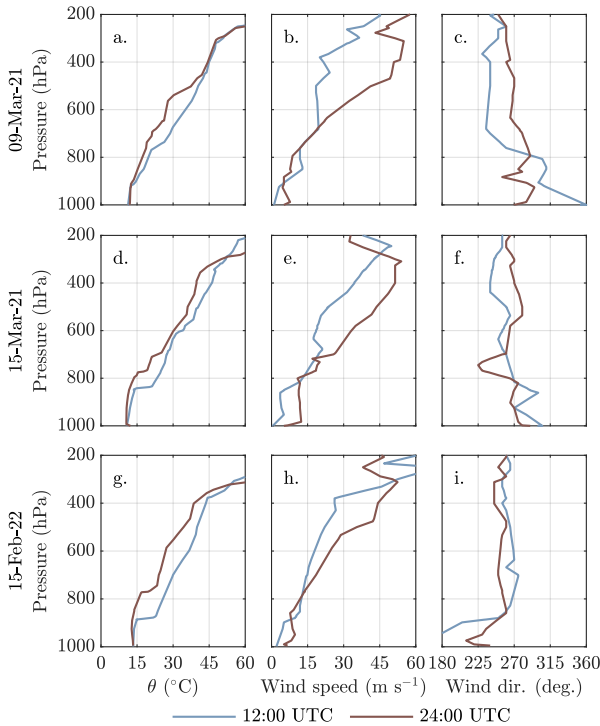
253 *a. Synoptic Situation*

254 We first describe the synoptic environments for the three dust events considered here. For all
 255 cases streamlines and heights of the 500 hPa pressure surfaces from NARR show an upper level low
 256 displaced to the northwest of the region of interest, with the lows' centers of action approximately
 257 located at 45° and -130°E on March 9, 2021 (Fig. 3a), and 40°N and -120°E on March 15, 2021
 258 and February 15, 2022 (Figs. 3b, c, respectively). For each case the elevated lows direct westerly



244 FIG. 3. Synoptic situations immediately preceding the dust outbreaks: March 9, 2021 at 18:00 UTC (3a, d),
 245 March 15, 2021 at 21:00 UTC (3b, e), and February 15, 2022 at 15:00 UTC (3c, e). Shown in the top row (3a–c)
 246 are maps of NARR 500 hPa wind speeds (shading), streamlines (black), and heights (yellow contours). Heights
 247 of the 500 hPa pressure surfaces are represented by the yellow contours at intervals of 5 dm, with the thick
 248 contour representing the 560 dm surface. The black box indicates the area shown in Fig. 1. Shown in the bottom
 249 row (3d–f) are maps of 850 hPa temperature (shading), sea level pressure (black), and vector winds (arrows).
 250 Cold fronts (blue) and surface lows (boxed “L”) locations are based on NOAA Weather Prediction Center surface
 251 analysis. Sea level pressure contours are hPa greater than 1000 hPa. The magenta shading represents the location
 252 of the Salton Sea. The horizontal extents of the maps in the top and bottom rows are not identical.

259 flow across the region of interest (black squares), with all exhibiting tightly packed height contours
 260 and cross barrier (i.e., westerly) wind speeds greater than 20 m s^{-1} . We note that that for the
 261 March 9 case the westerly flow is driven by both the broad low located to the north over the Pacific
 262 and an anti-cyclone located to the southeast (anti-cyclone not seen in Fig. 3a). Sea level pressure
 263 contours for these three cases show surface low pressure centers north of the Salton Sea and near
 264 exit regions of the the upper level jets, with trailing cold fronts pushing through the Salton Basin at
 265 approximately 18:00, 21:00, and 15:00 UTC (Figs. 3d, e, f, respectively). Temperatures and vector
 266 winds at 850 hPa imply low-level northwesterly cold air advection behind the fronts and westerly
 267 flow directed at the coastline and over the Salton Sea. The synoptic situations for these cases are
 268 similar to that described for dust outbreaks occurring on February 22, 2020 (Evan et al. 2022c)
 269 and March 14, 2018 (Evan 2019).



270 FIG. 4. Measurements from soundings made at the NKX station (see location in Fig. 1). Shown are vertical
 271 profiles of potential temperature θ (4a, d, g), wind speed (4b, e, h), and wind direction (4c, f, i) collected from
 272 radiosondes launched at 12:00 (light blue) and 24:00 (rust) UTC on March 9, 2021 (4a–c), March 15, 2021
 273 (4d–f), and February 15, 2022 (4g–i).

274 The characteristics of these mature cyclone wave and frontal systems (Fig. 3) generate unique
275 conditions that are favorable for trapping waves, including low-level cold air advection below a
276 westerly jet streak. For the March 9 case (Figs. 3a, d) the upper level trough is open and exhibits a
277 slight negative tilt. Vertical profiles of potential temperature θ and wind speed and direction made
278 from radiosondes launched from the NXX sounding station (see location in Fig. 1) at 12:00 UTC on
279 this day show a 5 C increase in θ in the 725-775 hPa layer (Fig. 4a), which is within a deeper layer
280 (700-800 hPa) of backing winds (Fig. 4c), implying low level cold air advection and cold frontal
281 passage. The sounding made 12 hours later on this day, and after the surface front had passed
282 over the Salton Sea region, shows lifting of the isentropic surfaces from 500-800 hPa (Fig. 4a),
283 indicating a deeper layer of cold air. The 30 m s^{-1} increase in wind speed from 300-500 hPa reflects
284 displacement of the associated jet streak over the region (Fig. 4b). The westerly flow throughout
285 much of the troposphere in the later sounding (Fig. 4c) reflects the strongly zonal nature of the jet
286 at this latitude, which results in part from the continued deepening and southward migration of the
287 low at -130°E and 45°N (not shown).

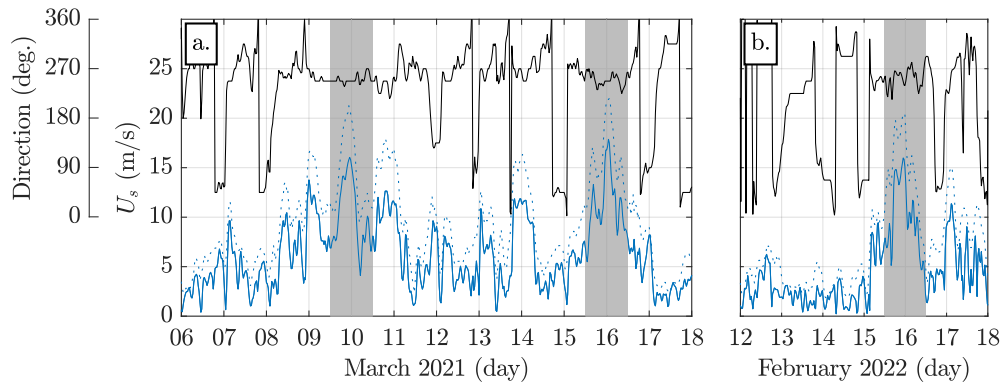
288 The low in the March 15 case (Figs. 3b, e) is better developed than that for March 9, exhibiting
289 a neutrally tilted trough digging down the western US coastline. The NXX soundings from this
290 day (Figs. 4d–f) are similar to those from March 9 in several ways, including a 6 C increase in θ at
291 850 hPa and a layer of backing winds from 800-850 hPa. The sounding made 12 hours later shows
292 lifting of the θ inversion layer to 775 hPa and the layer of backing winds to 775-825 hPa heights.
293 The later sounding also suggests warm air advection in the 750-600 hPa layer, as evidenced by the
294 veering flow from 750-600 hPa and similarity in θ at those heights over the 12-hour time period.
295 Similar to the March 9 case is the presence of a westerly jet with maximum wind speeds at 400-300
296 hPa.

297 Lastly the February 15 positively-tilted short wave trough (Fig. 3c) was a fast-moving system and
298 neither NXX sounding for this day exhibits clear signs of cold frontal passage (Figs. 4g–i). The
299 measurements indicate a large 8 C increase in θ at 870 hPa in the 12:00 UTC sounding, that lifts
300 to approximately 775 hPa 12 hours later, with cooling throughout the 400-900 hPa heights during
301 this time period. The latter sounding also shows an approximately 15 m s^{-1} increase in wind speed
302 during this period in the 500-400 hPa layer. Noting that the veering flow below 850 hPa may be

303 the result of surface friction rather than indicating warm air advection, both radiosondes suggest a
304 deep layer of positive zonal flow.

305 As we discuss in Section 4, these profiles all exhibit characteristics favorable to the generation
306 of trapped lee waves, including low-level cold air advection, with warm air advection aloft in the
307 February 15 case, strongly zonal (i.e., cross-barrier) flow, and positively sheared winds, especially
308 above the heights of the mountain ridges, which in Fig. 4 is approximately located in the 850-800
309 hPa range.

315 Within the Salton Basin the passage of these three frontal systems generated a similar response
316 in the surface meteorological conditions. During each the 30-minute averaged surface wind speeds
317 U_s and gusts measured at the field site exceeded 10 and 20 m s^{-1} , respectively, and were westerly
318 in direction (Fig. 5). The persistently westerly flow during the dust outbreaks is in contrast to
319 the typical patterns of wind speed and direction in the basin, which can be characterized as a
320 thermally-driven daytime upslope (easterly) and downslope (westerly) circulation forced by the
321 mountains that lie to the west of the site (e.g., March 6–8, March 12–14 Fig. 5a).

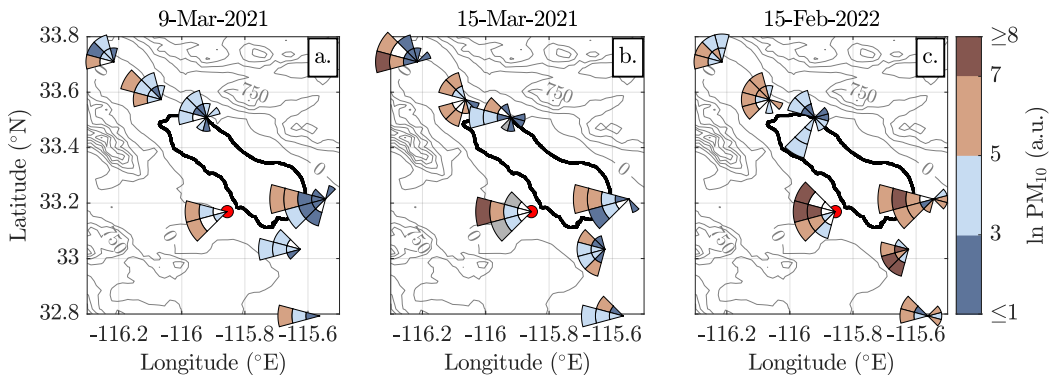


310 FIG. 5. Time series of surface meteorological measurements made from the field site during March 2021 (5a)
311 and February 2022 (5b). Plotted are 30-minute averaged values of surface wind speed U_s (blue solid line), wind
312 gust speed (blue dotted line), and wind direction (black solid line), with the value of direction indicated by the
313 left-most vertical axis. The gray shaded regions indicate 24-hour periods commencing at 12:00 UTC on March
314 9 and March 15, 2021, and February 15, 2022, during which the dust outbreaks occurred.

322 *b. Observations of Dust*

323 We next consider the spatial and temporal variability of the dust generated by the high winds
 324 present over the Salton Basin. In order to simultaneously visualize wind speed and direction and
 325 PM_{10} we generated modified versions of wind roses. For each, the station physical location is at
 326 the center point of the rose. Concentric circles indicate wind speed ranges, where the area from
 327 the center point to the first concentric circle represents wind speeds in the range of $0-4 \text{ m s}^{-1}$, the
 328 area from the first to the second circles represents wind speeds in the range of $4-8 \text{ m s}^{-1}$, and so
 329 on in increments of 4 m s^{-1} . The radial divisions represent wind direction. Shading refers to the
 330 natural logarithm of the maximum hourly PM_{10} measured for a given wind speed and direction
 331 range, where $\ln PM_{10}$ values ≥ 5 are above the US EPA 24-hour air quality standard of $150 \mu\text{g}$
 332 m^3 . The data displayed in Fig. 6 corresponds to the time periods highlighted in gray in Fig. 5.
 333 Hourly-averaged PM_{10} and wind speed measurements are used to generate these plots.

340 For all of three cases PM_{10} values exceeding $150 \mu\text{g m}^{-3}$ ($\ln PM_{10} \geq 5$) were observed for at
 341 least five of the seven stations, with PM_{10} exceeding $150 \mu\text{g m}^{-3}$ at all stations during the March
 342 15 case (Fig. 6b). At the northernmost station the strongest wind speed and PM_{10} values occur
 343 during northwesterly winds, likely due to flow channeling through Banning Pass (Ryerson et al.



334 FIG. 6. Modified wind roses indicating peak concentrations of PM_{10} during the three dust outbreaks. Shown
 335 in each map are roses (see text for description) made from measurements collected during the dust outbreaks on
 336 March 9 (6a) and March 15, 2021 (6b), and February 15, 2022 (6c). Gray shaded rose sections in 6b indicate
 337 wind speeds and directions for which corresponding PM_{10} measurements were missing. The gray contours
 338 represent surface elevations at intervals of 250 m, and the thick black line represents an estimate of the Salton
 339 Sea shoreline in March 2021. The location of the field site is indicated by the red circular marker.

2013), which sits at the northern terminus of the Salton Trough (Fig. 1b). Further to the south the strongest wind speeds and PM_{10} values correspond to increasingly westerly flow, which reflects the widening of the basin and the proximity of the Anza desert, which lies to the west of the Salton Sea and is upwind of the field site (Fig. 1a). Based on the prevalence of measurements for which $\ln \text{PM}_{10} \geq 5$, the February 15 event exhibited the largest number of high surface dust concentrations (Fig. 6c), and the March 9 case exhibited the lowest surface dust concentrations (Fig. 6a).

Retrievals of aerosol optical depth τ from the CIMEL sun photometer show maximum aerosol optical depths of approximately 0.4 on March 9 and March 15, and 0.45 on February 15 (Fig. 7a, b, c, respectively). The number of CIMEL τ retrievals is related to the presence of daytime clear-sky conditions; cloud cover was present over the site prior to 18:00 UTC on March 9, and there was

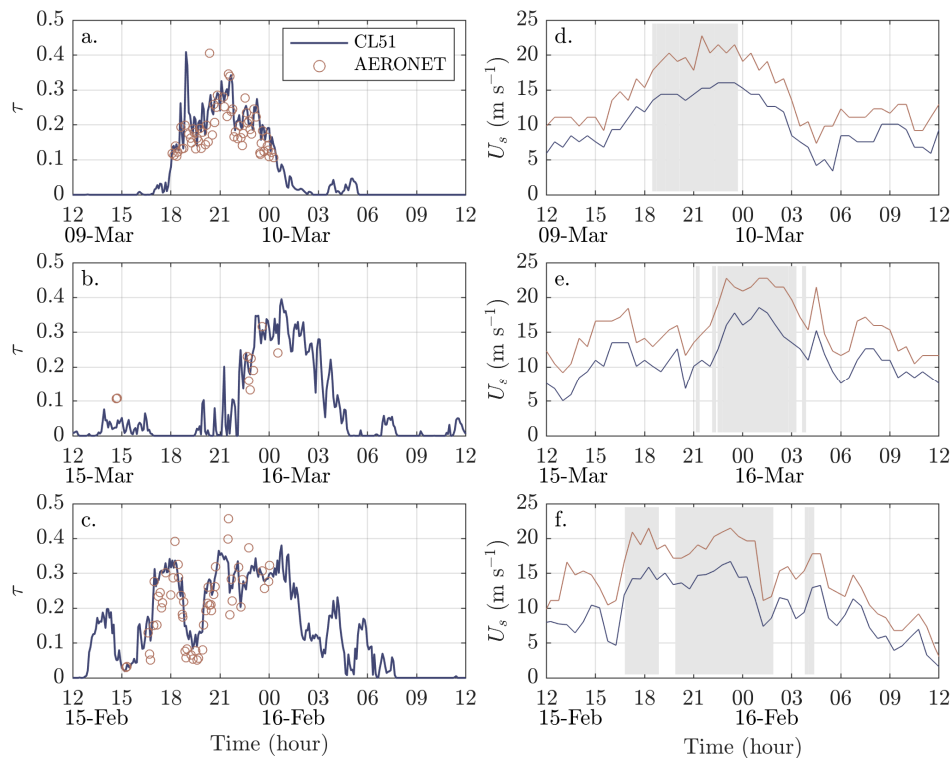


FIG. 7. Aerosol optical depth τ retrievals and surface wind speeds measured at the field site during the three dust cases. Shown in 7a–c are time series of τ retrieved from the CL51 (solid line) and the AERONET sun photometer (circles) during each of the three dust outbreaks. Shown in 7d–f are corresponding measurements of surface wind speeds (blue) and gusts (red-orange), with time periods during which $\tau \geq 0.2$ indicated by the gray shading.

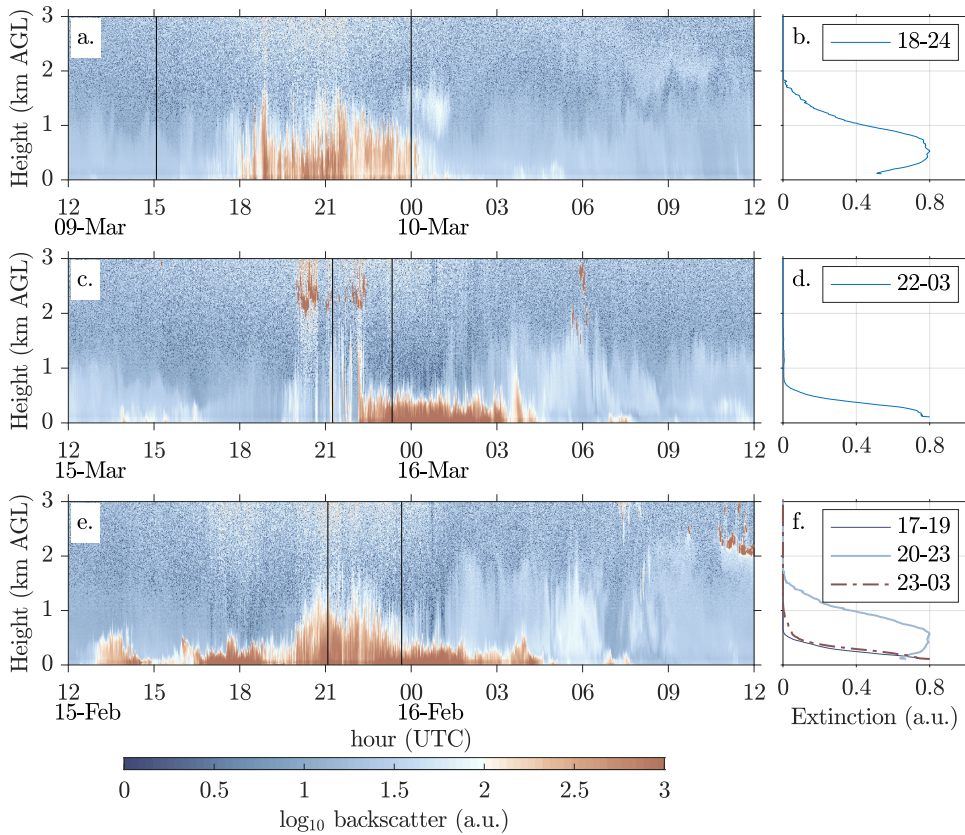
359 intermittent cloud cover throughout the March 15 event, whereas the sky was clear on February
360 15 (see animations M1–3 in the Supplement). Post-processed values of τ retrieved from the CL51
361 are broadly in agreement with those from AERONET, and thus can be used to estimate τ in the
362 subcloud layers and at nighttime. If we arbitrarily define a dust outbreak as $\tau \geq 0.2$, from these
363 data the duration of the March 9 event was approximately 5 hours (Fig. 7a, 18:35 to 23:35 UTC),
364 the March 15 event lasted 5.5 hours (Fig. 7b, 22:15 to 03:45 UTC), and the February 15 event had
365 a duration of 11.17 hours (Fig. 7c, 17:05 to 04:15 UTC), although the latter event was punctuated
366 by distinct periods of $\tau < 0.2$ at 15:00, 19:30, and 03:00 UTC.

367 A comparison of measurements of τ and the corresponding surface wind speed U_s suggests that,
368 in general, $\tau \geq 0.2$ when the surface wind speeds and gusts exceed 9 and 17 m s^{-1} , respectively
369 (gray shading in Figs. 7d–f). Although for the February 15 case there are several time periods
370 during which $\tau > 0.2$ but wind speeds are well below 9 m s^{-1} , and when $\tau < 0.2$ but wind speeds
371 are above 9 m s^{-1} (Fig. 7f). For these cases dust over the field site is emitted from the upwind
372 desert region to the west (see animations M1–3 in the Supplement), and as discussed in Section
373 4, decoupling of τ and U_s in the February 15 case may be due to the influence of non-stationary
374 trapped waves.

380 Measurements of backscatter made from the CL51 ceilometer located at the field site provide
381 information about the vertical structure of the dust storms. Plotted in Fig. 8 are \log_{10} of the
382 ceilometer range corrected backscatter signal within the lower 4 km of the atmosphere for 24 hour
383 periods commencing at 12:00 UTC on March 9 (Fig. 8a) and 15, 2021 (Fig. 8c) and February 15,
384 2022 (Fig. 8e). Values of \log_{10} backscatter that are greater than 2 are a reasonable indication of
385 the presence of suspended dust based on comparisons with aerosol optical depth retrievals from
386 the collocated sun photometer (Evan et al. 2022a), and backscatter values greater than 2 that are
387 located well above the surface indicated the presence of clouds (e.g., 2–3 km AGL at 20:00 UTC
388 on March 15 in Fig. 8c).

389 The CL51 data show that for all three cases dust is confined to a layer below 2 km AGL, but
390 that the depth of the dust plume and the vertical distribution of the aerosols vary both between
391 events and within the individual dust outbreaks. For example, the dust outbreak on March 9 is
392 characterized by a plume having depth 1–2 km AGL (Fig. 8a) with extinction values peaking at
393 500 m AGL (Fig. 8b). For the March 15 case dust is confined to the shallow layer of 300–700

394 m AGL (Fig. 8c), with extinction peaking at the lowest retrievable level of 100 m AGL (Fig. 8b).
 395 Differences in the shapes of the extinction profiles for the March 9 and 15 cases explain why surface
 396 PM_{10} measurements for the March 15 case were far greater than those for March 9 (Figs. 6a, b)
 397 although the dust optical depth for these two events are nearly identical in magnitude (Figs. 7a, b).
 398 The ceilometer data for February 15 exhibits distinct periods of dust layer depths, ranging from
 399 600 m to 2 km AGL (Fig. 8e). We consider the factors affecting the vertical distribution of dust in
 400 Section 4.



375 FIG. 8. Ceilometer backscatter and extinction profiles from CL51 measurements made at the field site. Shown
 376 are vertical profiles of the log of the CL51 range corrected signal during the dust outbreaks on March 9 & 10
 377 (8a) and 15 & 16, 2021 (8c), and February 15 & 16, 2022 (8e). The vertical black lines in each represent times
 378 radiosondes were launched at the site (Fig. 9). Plotted in 8b, d, f are extinction profiles averaged over the time
 379 period indicated in the legends (in hours UTC), and corresponding to the days indicated in the adjacent panels.

401 *c. Terrain Forced Flow*

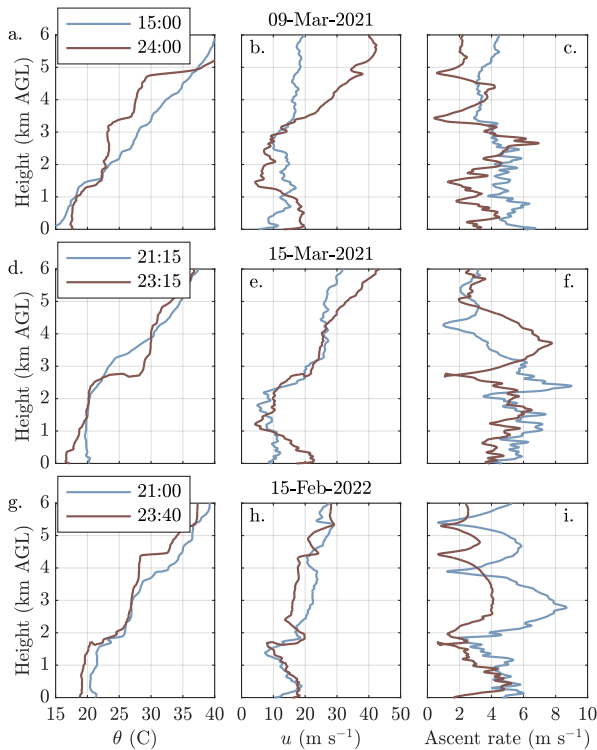
402 Having provided an overview of the synoptic situation for these dust events and examined the
403 physical characteristics of the airborne dust, we next consider the role of orography in generating
404 the high winds that gave rise to the dust outbreaks. The mountain range that lies immediately to
405 the west of the Salton Basin (the Peninsular Mountains) is north-south oriented and rises gradually
406 from the Pacific Ocean to peak heights up to 3 km, with steep eastern slopes that plunge into the
407 sub-sea level Salton Basin (Fig. 1b, see also Fig. 5 in Evan 2019). Given the characteristics of the
408 Peninsular Mountains (which hereafter we also refer to as the upwind barrier), wind in the zonal
409 direction is cross-barrier and thus westerly flow has the potential to generate strong downslope
410 windstorms in the lee of these mountains (Durrán 1990). In order to elucidate the influence of the
411 orography on the lee-side flow we examine radiosondes launched from the field site on each of the
412 days in question and output from WRF simulations of these events.

417 A profile of potential temperature θ obtained from a radiosonde launched prior to the March
418 9 dust outbreak at 15:00 UTC (07:00 local time) shows the remnants of a nocturnal inversion,
419 with θ increasing from 15 to 18 C from the surface to 1.5 km AGL, which is then capped by an
420 approximately 4 C inversion layer, with θ increasing steadily above (Fig. 9a). The corresponding
421 cross-barrier wind speeds u vary between 10 and 20 m s⁻¹ throughout the lower 6 km of the
422 atmosphere (Fig. 9b). A radiosonde released at 24:00 UTC on this day (16:00 local time), which
423 is during the dust outbreak (Fig. 8a), shows 5 C warming at the surface relative to the 15:00 UTC
424 sounding but little change in the 1-1.5 km layer. If we define the top of the convective boundary
425 layer as the height at which θ equals the surface temperature, which is reasonable given that the
426 layer is dry, the depth of the convective boundary layer during the dust outbreak is 1.5 km, which
427 is consistent with the depth of the dust layer during this event (Fig. 8b).

428 During the March 9 dust outbreak the profile of u can be characterized as consisting of a low-level
429 jet having peak wind speeds of 20 m s⁻¹ from just above the surface to a height of 1 km AGL, and
430 a wind speed minimum of 5 m s⁻¹ at the height of the inversion at 1.5 km AGL (Fig. 9b). The
431 height of the wind speed minimum and 4 C inversion are also located at a minima in the balloon's
432 ascent rate, which is in contrast to the more constant ascent rate prior to the dust outbreak (Fig. 9c).
433 Inversions apparent in the profile of θ at heights of 1.5, 3.5, and 4.9 km AGL are coincident with
434 minima in ascent rate and thus the magnitudes of these inversions are affected by the reductions in

435 the radiosonde’s vertical velocity. Minima in the ascent rate also indicate the presence of waves,
 436 similar to cases examined in Strauss et al. (2016). The presence of waves is also apparent in
 437 measurements from other soundings made during these events (Figs. S6, S12).

438 Radiosondes launched immediately prior to and during the dust outbreak on March 15, 2021
 439 show some similar characteristics to those from the March 9 case. The vertical profile of θ prior to
 440 the dust outbreak at 21:15 UTC (14:15 local time, Fig. 8c) suggests a well-mixed boundary layer
 441 extending from the surface to approximately 2 km AGL (Fig. 9d) with u near 10 m s^{-1} throughout
 442 this depth (Fig. 9e). In contrast, the sounding made during dust outbreak (23:20 UTC, 16:20 local
 443 time) is accompanied by cooling of approximately 3 C in the lower 500 m of the atmosphere (Fig.
 444 9d) and a pronounced low level jet characterized by peak wind speeds of 23 m s^{-1} at heights of
 445 100-300 m AGL and a wind speed minimum of 5 m s^{-1} at 1.25 km AGL. The radiosonde ascent



413 FIG. 9. Sounding measurements from radiosondes launched from the field site on March 9 2021 (9a–c), March
 414 15 2021 (9d–f), and February 15 2022 (9g–i). Plotted are radiosonde profiles of potential temperature θ (9a,d,g),
 415 zonal wind speed u (9b,e,h), and balloon ascent rate (9c,f,i). Times of the radiosonde launches (UTC hours) are
 416 indicated in the legends in 9a,d,g.

446 rates implies wave activity in the atmosphere, with a minimum in ascent rate at 2.8 km AGL (Fig.
447 9f) that is located at the height of a nearly 10 C inversion (Fig. 9d). We again note that this apparent
448 inversion is heavily influenced by the nearly horizontal motion of the balloon at this height.

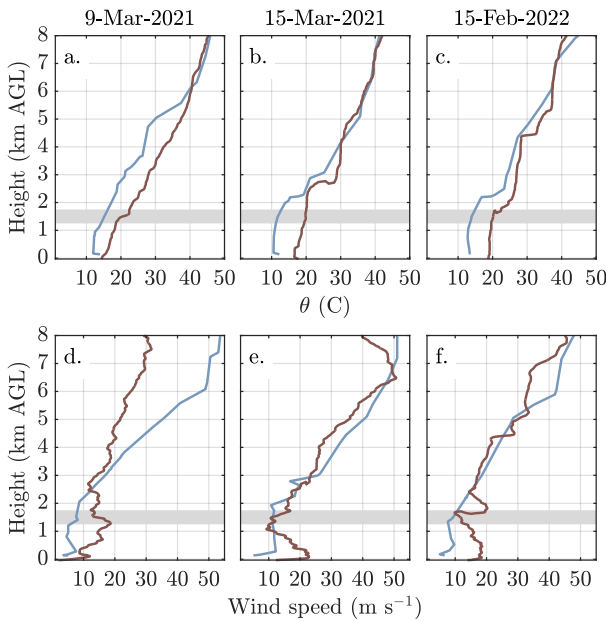
449 The low-level cooling accompanying the onset of high wind speeds helps explain the observed
450 shallow depth of the dust layer on March 15, relative to the March 9 case (Fig. 8d). These features
451 of the March 15 dust outbreak are similar to those for a dust outbreak that occurred on February
452 22, 2021, which was generated by spillover precipitation and evaporative cooling over the desert
453 to the west of the research site (Evan et al. 2022c). Here we noted no spillover precipitation for the
454 March 15 case and thus any density-current like features are due to cold post-frontal downslope
455 flow (Karyampudi et al. 1995; Koch et al. 1991).

456 For the February 15, 2022 case no radiosondes were launched prior to the dust outbreak, although
457 the radiosondes measurements shown in Figs. 9g–l do correspond to periods of differing heights
458 of the dust plume (Fig. 8e). Profiles of potential temperature made at 21:00 UTC (13:00 local
459 time) and 23:40 UTC (15:40 local time) show an inversion just below 2 km AGL (Fig. 9g). For the
460 earlier time we estimate a convective boundary layer depth of 1.6 km, which is consistent with the
461 depth of the dust layer averaged from 20:00–23:00 UTC (Fig. 8f). For the 23:40 sounding there is
462 relative cooling of approximately 1.5 C in the lower 1.8 km of the atmosphere, and 2.0 C at the
463 surface. This change in the θ profile suggests that the depth of the convective boundary layer is
464 reduced to 1 km AGL, consistent with the depth of the dust layer averaged from 23:00–03:00 UTC
465 (Fig. 8f).

466 Similar to the March 9 and 15 cases, zonal wind speeds from radiosondes launched during the
467 dust outbreak on February 15 show low level jets, with speed maxima of 18 m s^{-1} located at heights
468 of 400–500 m AGL, and wind speed minima of 8 m s^{-1} at 1.5–1.75 km AGL (Fig. 9j). For these
469 cases we also find minima in radiosonde ascent rates that are coincident with inversions present
470 in the θ profiles, including at 1.9, 3.9, and 5.4 km AGL for the 21:00 UTC sounding (13:00 local
471 time), and 1.7, 4.5, and 5.3 km AGL at 23:40 UTC (15:40 local time, Fig. 9k), again reflecting the
472 presence of waves in the overlying atmosphere.

473 We again utilize radiosondes made from the NKX sounding station located near the coast (Figs. 1,
474 3) in order to understand the factors that give rise to these downslope windstorms via examination of
475 radiosondes released at 24:00 UTC from this location and the nearest in time radiosondes released

481 from the field site near the Salton Sea (Fig. 10). According to Mayr and Armi (2010) lee-side flow
 482 will plunge to the floor of the basin if the potential temperature of the air flowing over the ridge is
 483 cooler than that of the down-barrier surface. The heights of the ridgeline upwind of the field site
 484 are in the range of 1.25 to 1.75 km AMSL (gray shaded band in Fig. 10), and the upwind (NKX)
 485 potential temperatures at these heights (Figs. 10a–c, light-blue) are all lower than the downwind
 486 values of θ below 1.25 km (Figs. 10a–c, rust). Vertical profiles of wind speed from the NXX
 487 soundings suggest upwind orographic flow blocking, as evidenced by wind speeds below 1.25 km
 488 in the range of 5-12 m s⁻¹ that are in contrast to the high wind speeds downwind of the barrier
 489 (Figs. 10d–f). Above the heights of the ridge the upwind and downwind wind speed profiles are
 490 similar, with the exception of the jet at 1.75-2.5 km in the February 15 downwind profile (Fig. 10f),
 491 which is due to the influence of wave activity on the radiosonde ascent rate. These differences in
 492 the soundings upwind and downwind of the barrier are consistent with isentropic drawdown of the

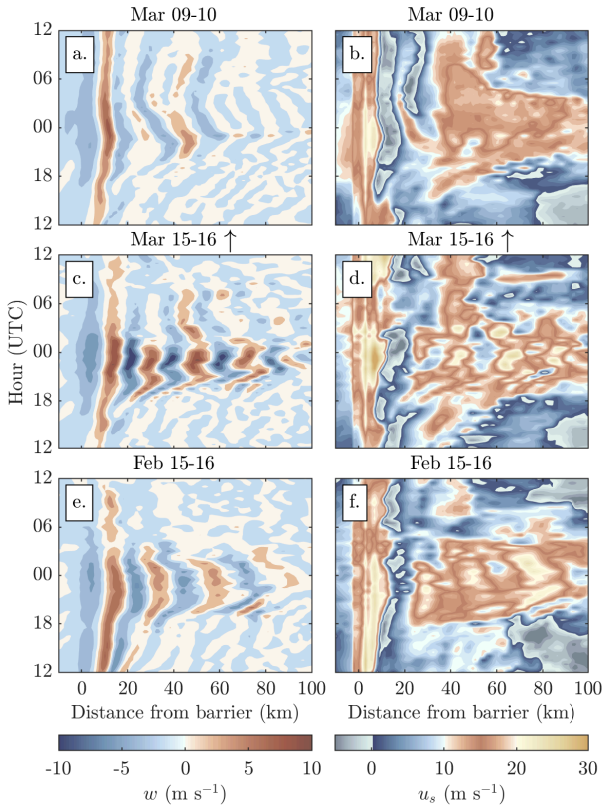


473 FIG. 10. Radiosonde profiles of θ (top row) and wind speed (bottom row) from San Diego, CA (NKX), which
 474 is upwind of the barrier (light-blue) and from the field site that is located near the Salton Sea (rust). The heights
 475 of the mountain ridge represented by the gray shaded band in each panel. Profiles are shown for the 24:00 UTC
 476 soundings from San Diego and the radiosondes launched closest to this time near the Salton Sea (i.e., the later
 477 sounding times in Fig. 9) for March 9 (10a,d) and March 15, 2021 (10b,e), and February 15, 2022 (9c,f).

493 cross-barrier flow at or above the the height of the ridgeline and a lee-side downslope windstorm
 494 Durran (1990).

495 *d. Numerical Simulations with WRF*

500 In order to provide broader context to the in-situ measurements we also examine output from
 501 numerical simulations using WRF, focusing on model output along the 33.25°N latitude transect
 502 for the innermost model domain (Fig. 2). The WRF simulations reproduced several aspects of
 503 the surface and upper air measurements, including strong westerly surface wind speeds during the
 504 dust events (Fig. S1). However, at least at the field site, the simulated timing of the onset and
 505 termination of high wind speeds did not line up with observations, and for several cases waves in



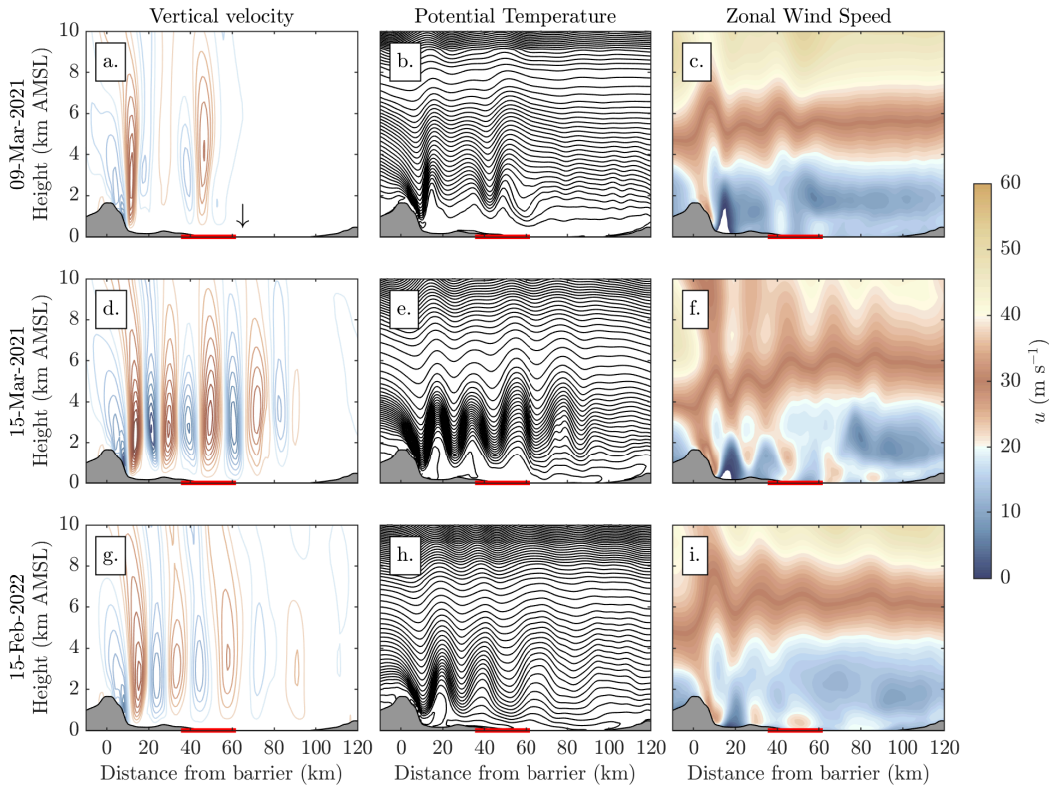
496 FIG. 11. Hovmöller diagrams of 3-4 km height averaged vertical velocity w (11a,c,e) and surface zonal wind
 497 speed u_s (11b,d,f) along the 33.25°N latitude transect during the March 9 2021 (11a–b), March 15 2021 (11c–d),
 498 and February 15 2022 (11e–f) dust outbreaks. The upward pointing arrows in 11a,b indicate the location of the
 499 field site. Reference orography along this transect can be found in Fig. 12.

506 the model appeared to be out of phase with wave activity implied by changes in the radiosonde
507 ascent rate (Figs. S2–S13). As such, WRF output is used to understand the general behaviour of
508 the downslope flow and trapped waves in the Salton Basin, rather than to explain the timing of
509 specific aspects of these events.

510 Hovmöller diagrams of vertical velocity w averaged over the 3-4 km layer during 24-hour time
511 periods starting at 12:00 UTC on March 9 (Fig. 11a) and March 15, 2021 (Fig. 11c), and February
512 15, 2022 (Fig. 11e) indicate the presence of trapped lee waves during the periods of observed high
513 winds and dust (Fig. 7). For all three cases and during the entire 24-hour time period downslope
514 flow is simulated along the lee side slopes of the upwind barrier (the barrier ridge is located at the
515 0 km point on the horizontal axis and flow downwind of the barrier is located at positive horizontal
516 distances, a transect of the orography is found in Fig. 12), and then vertical ascent at 10 km distance
517 from the barrier. This type of plunging flow and downwind jump has been the focus of research on
518 high wind events and dust storms in the Owen's valley (e.g., Grubišić et al. 2008). Indeed, similarly
519 constructed Hovmöller diagrams of u at the lowest model level indicate the strongest surface winds
520 ($u > 20 \text{ m s}^{-1}$) along the lee-side slopes for all three cases (Figs. 11b,d,f). However, distinct from
521 the narrow Owen's valley, in the Salton Basin the terrain of the first 35 km downwind of the barrier
522 is vegetated and generally non-emissive, and as such the high winds associated with the flow at the
523 base of the barrier do not produce dust here.

524 A distance-height transect of model output vertical velocity w (Figs. 12a,d,g) and dry isentropes
525 (Figs. 12b,e,h), averaged over two-hour time periods during which the waves are approximately
526 stationary, indicate the existence of trapped waves in all three cases. The weakest wave activity is
527 seen in the WRF output for March 9, where the magnitude of the vertical wind speeds drop below 1
528 m s^{-1} at a distance of approximately 60 km from the mountain ridge (Fig. 12a). The March 15 case
529 exhibits the strongest wave activity, with waves of quasi-regular wavelength 20 km and vertical
530 velocity magnitudes as large as 5 m s^{-1} at a barrier distance of 85 km (Fig. 12d). The February 15
531 case also shows strong wave activity throughout the model domain, but of smaller magnitude and
532 longer wavelength than that for March 15 (Figs. 12g). For all three cases the waves are evanescent
533 above approximately 6 km height (Fig. 12b,e,h), due to changes in static stability and vertical wind
534 shear in the flow upstream of the orography (Fig. 10).

544 Relevant to understanding the influence of trapped waves on dust emission and transport is their
 545 effect on surface wind speed u_s . Firstly, from the Hovmöller diagrams in Fig. 11 the strongest
 546 wind speeds are in-general found along the leeside slopes, with weak and even reversed flow just
 547 downwind of the barrier base, indicative of flow separation and a rotor circulation (Doyle and
 548 Durran 2002). Further downwind of the barrier the strongest surface wind speeds ($u_s > 20 \text{ m s}^{-1}$)
 549 are associated with the presence of trapped waves. For example, in the February 15 case plunging



535 FIG. 12. WRF output along the 33.25°N latitude transect averaged over simulation times 21:00–23:00 UTC on
 536 March 9, 2021 (12a–c), 22:00–24:00 UTC on March 15, 2021 (12d–f), and 22:00–24:00 UTC on February 15,
 537 2022 (12g–i). Horizontal distance is given in km from the peak of the upwind orography. Plotted in 12a,d,g are
 538 vertical wind speeds w in contour intervals of 1 m s^{-1} , with warm colors representing positive w and cool colors
 539 representing negative w , and where the 0 m s^{-1} isotach is not plotted. Plotted in 12b,e,h are lines of constant θ
 540 in 1 C intervals. Shown in 12c,f,i is u , where the white shaded region at the downwind base of the orography
 541 indicates reversed flow ($u < 0$). The downward pointing arrow in 12a represents the location of the field site.
 542 The red horizontal line in all figure panels represents the approximate locations of dust emission that are upwind
 543 of the field site.

550 flow along the lee-side slopes (0-10 km) produce horizontal surface wind speeds near 30 m s^{-1}
 551 from 12:00–00:00 UTC (Fig. 11f). Prior to the development of trapped waves at approximately
 552 18:00 UTC (Fig. 11e) surface wind speeds at barrier distances greater than 20 km are below 10 m
 553 s^{-1} . As lee waves develop surface wind speeds greater than 25 m s^{-1} are found as far as 90 km
 554 from the barrier. In general and for these cases, since dust emission primarily occurs at barrier
 555 distances greater than 35 km, significant dust uplift in the basin would only occur after lee wave
 556 onset.

557 The effect of wave activity on surface wind speed u_s is apparent in the cross-sections of zonal
 558 wind speed (Fig. 12c,f,i). Perturbations in u_s are out of phase with horizontal gradients in w
 559 and are in phase with θ , which is due to surface pressure minima under the regions of strongest
 560 upward vertical velocity, and surface pressure maxima located under the strongest downdrafts
 561 (Nappo 2013). For all three cases the strongest surface wind speeds are all found under the wave
 562 troughs. Although the speed of the plunging flow along the lee side slopes is very similar for all
 563 three cases, surface wind speeds further downwind of the barrier (distances greater than 20 km)
 564 are the weakest in the March 9 case, in which the trapped waves are less pronounced and dissipate
 565 at barrier distances greater than 50 km, and are the strongest downwind during the March 15 case,
 566 in which the waves are still coherent at barrier distances greater than 80 km.

567 4. Discussion

568 Orographically forced waves can become trapped in a layer near the surface if the static stability
 569 or curvature of the wind shear change with height such that waves cannot propagate upward and
 570 are thus evanescent with height. Wave trapping can be predicted by vertical changes in the Scorer
 571 parameter l^2 upwind of the barrier, which is defined as (Scorer 1949)

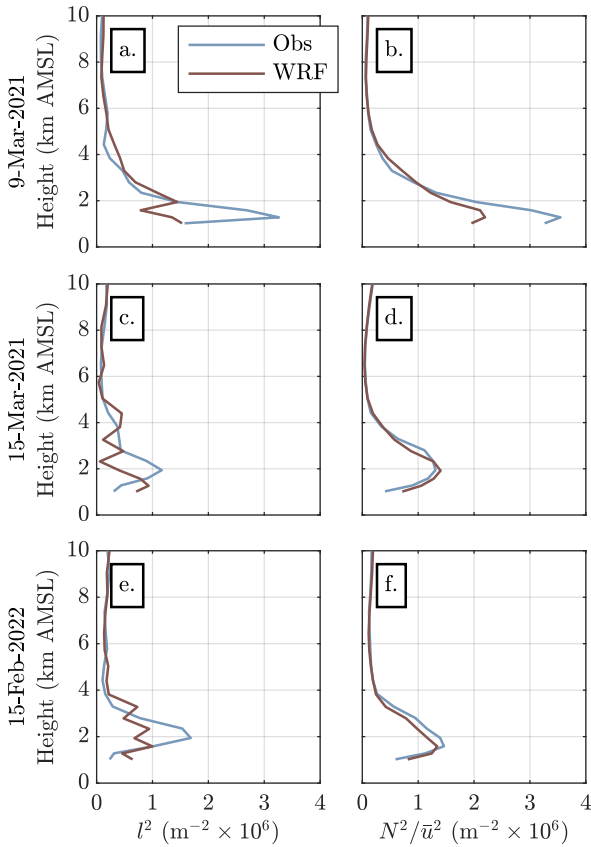
$$l(z)^2 = \frac{N^2}{\bar{u}^2} - \frac{1}{\bar{u}} \frac{d^2 \bar{u}}{dz^2} \quad (1)$$

572 where \bar{u} indicates the cross-barrier wind speed and N the Brunt-Vaisala frequency, both of which
 573 are resolved in z . For example, if we consider the atmosphere to consist of uniform lower and
 574 upper layers, orographically forced gravity waves become trapped in the lower level for

$$l_L^2 > k^2 > l_U^2$$

575 where k is the horizontal wavenumber of the trapped waves and l_L^2 and l_U^2 are Scorer parameters
 576 of the lower and upper layers, respectively. For the idealized case of constant wind speed with
 577 height in the upwind atmosphere these conditions are satisfied if N^2 of the upper layer is less than
 578 that of the lower layer, meaning that the buoyancy restoring force in the upper layer N_U^2 is too weak
 579 to support gravity waves for which $k^2 > N_U^2/\bar{u}^2$. Thus wave energy remains trapped in the lower
 580 layer.

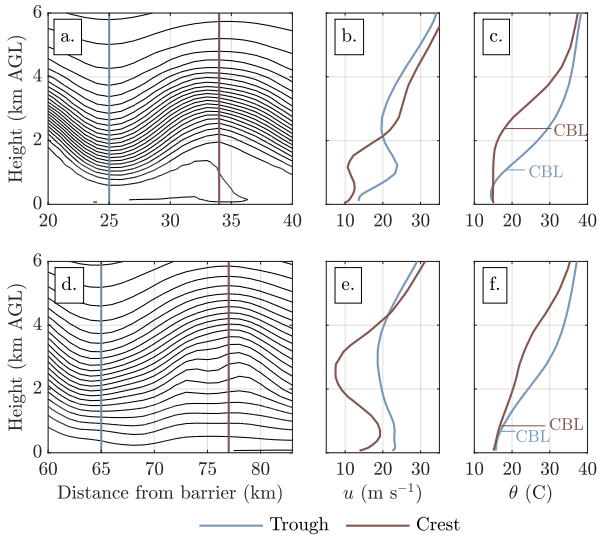
586 Plots of l^2 for the 24:00 UTC soundings made upwind of the barrier at the NKX site (see location
 587 in Fig. 1) show a reduction in l^2 with height for all three cases (Fig. 13). For March 9, l^2 peaks low



581 FIG. 13. Changes in the Scorer parameter with height. Plotted in the left-hand column panels is the Scorer
 582 parameter l^2 (Eq. 1) calculated from the 24:00 UTC soundings made from the NKX station (blue) and output
 583 from the WRF simulations (rust), for the dates indicated at left. Plotted in the right-hand columns is the l^2
 584 stability term (first term on the right-hand-side of Eq. 1), for the same data. Only values above 1 km are shown
 585 due to the blocked flow below this height (e.g., Fig. 10).

588 in the atmosphere, at a height of 1.3 km (Fig. 13a) and reaches a minimum at 4 km. For the other
 589 two cases l^2 peaks slightly higher in the atmosphere at 2 km, and reaches a minimum at 5.8 km
 590 (Fig. 13c) and 4.5 km (Fig. 13e). Profiles of the first term on the right-hand-side of Eq. 1 suggest
 591 that variations in l^2 are primarily driven by reductions in static stability above 2 km (Fig. 13b, d, f),
 592 since in all three cases \bar{u} increases nearly monotonically with height above the barrier (Fig. 10d–f).

593 In the model the reductions in l^2 with height are not as large as in the observations (Fig. 13a,c,e).
 594 This difference is due to discrepancies between the observed and simulated shear profiles as there
 595 is generally good agreement in the l^2 stability terms. We note that for the March 9 case the modeled
 596 stability term does not drop off as strongly with height as does that from observations (Fig. 13b),
 597 and thus it is plausible that the model is under predicting trapped wave activity for the three cases
 598 considered here.



599 FIG. 14. Changes in model zonal wind speed u and potential temperature θ with height for different wave
 600 phases and proximity to the surface. Plotted in 14a and 14d are contours of isentropic surfaces at 1 C intervals
 601 from the WRF output shown in Fig 12e (March 15, 2021 case) at barrier distances of 20-40 km (14a) and 60-83
 602 km (14f), where the vertical blue and rust colored lines in 14a,d indicate the locations of the wave troughs and
 603 ridges used to generate the profiles in the other figure panels. In 14b,e are profiles of cross-barrier wind speed
 604 u corresponding to the wave troughs (blue) and ridges (rust). Descriptions of the plots in 14c,f are the same
 605 as for 14b,e except that θ is plotted, and where the horizontal lines indicate the model-calculated height of the
 606 convective boundary layer (CBL).

607 Based on the measurements and model output presented here we suggest several characteristics
608 of dust storms generated by trapped waves. The first is the presence of a low-level jet (Fig.
609 10d–f), which is relevant in terms of dust production, advection, and dispersion due to the strong
610 wind speeds characterizing the jet and potential for vertical mixing at the shear inflection points
611 (i.e., where $d^2u/dz^2 = 0$). Pressure perturbations associated with wave phase generate positive
612 and negative horizontal wind speed perturbations under the wave troughs and crests, respectively
613 (Durrán 1986), resulting in vertical profiles of horizontal wind speeds u that resemble a low level
614 jet at the base of the wave trough or at the surface under a wave crest. The effect of wave phase
615 on vertical profiles of wind speed can be readily seen in the output from the WRF simulations
616 for the March 15 case (Fig. 12d–f), averaged from 22:00–24:00 UTC. Focusing on one cycle of
617 the simulated wave over barrier distances of 20–40 km (Fig. 14a), the simulated zonal (i.e., cross-
618 barrier) wind speed u is stronger under the wave crest than under the trough, from the surface up
619 to a height of 2 km AGL (Fig. 14b), which is the height where the isentropes above the trough start
620 to spread vertically. Under the wave trough u increases by 10 m s^{-1} from the surface to the base of
621 the wave at 1 km AGL. Under the crest there is a local maximum in u at approximately 500 m AGL
622 above which u decreases by 2 m s^{-1} to the local minimum at 1.3 km AGL. As such, the low-level
623 jet under the wave trough is more pronounced than that for the crest and has a nose located at the
624 base of the wave, while that under the crest is weaker with a nose located close to the surface.

625 For the same WRF simulation but at barrier distances of 60–83 km (Fig. 14d), possibly more
626 representative of the environment over the field site, the simulated wave is evanescent to the surface.
627 Here u is greater under the wave trough than the crest up to a height of 4 km AGL (Fig. 14e), which
628 for the trough is the height above which the isentropic surfaces start to spread vertically. While
629 there is no obviously discernible low-level jet under the wave trough, under the crest there is a
630 greater than 10 m s^{-1} reduction in u from the local maximum at 500 m up to the minimum at 2.5
631 km AGL, above which the isentropes become more tightly packed, signifying the wave base. The
632 similarity between the low-level jet under the wave crest in Fig. 14e and the wind speed profiles
633 in the soundings made during the dust outbreaks (Fig. 9b,e,h) raise the possibility that the site is
634 often located under wave crests during trapped wave events.

635 We suggest that another characteristic of dust storms generated by trapped lee waves is the
636 variable convective boundary layer and thus dust layer depths, which are dependant upon the phase

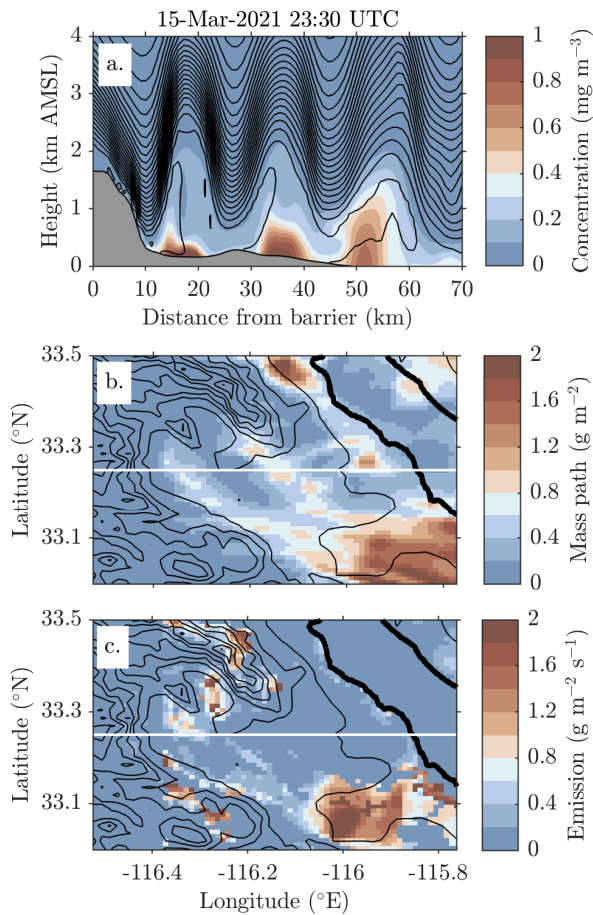
637 and proximity to the surface of the overlying wave. Returning to the WRF output from the March
638 15 case and barrier distances of 20-40 km (Fig. 14a), under the wave trough isentropes are displaced
639 downwards towards the surface, resulting in a modeled boundary layer height of 1 km AGL (Fig.
640 14c). In contrast, under the wave crest isentropic surfaces are displaced upwards such that θ is little
641 changed from the surface up to nearly 2 km AGL, with a corresponding boundary layer height of
642 2.4 km AGL. When considering distances of 60-83 km from the barrier (Fig. 14d) there is little
643 difference in the vertical distribution of θ under the wave trough and crest in the lower 1 km of the
644 atmosphere due to the proximity of the wave to the surface, with each exhibiting similar boundary
645 layer heights of 0.7 and 0.8 km AGL, respectively (Fig. 14f), which are more shallow than those
646 for the previous case. The relatively shallow simulated boundary layers in Fig. 14f may explain
647 why for the three cases considered here the observed dust layer depths are shallow (Fig. 8), and the
648 surface PM_{10} concentrations are high (Fig. 6).

655 We further consider the effect of wave phase on dust layer depth via simulations with WRF-
656 Chem. A transect of dust concentration from WRF-Chem for the March 15 case at 23:30 UTC and
657 for the first 70 km downwind of the barrier indicates that the depth of the dust layer closely follows
658 the curvature of the isentropic surfaces that define trapped wave base (Fig. 15a). Furthermore,
659 the highest dust concentrations are found under the wave crests, where the simulated zonal and
660 cross-barrier wind speeds are near zero or negative (Fig. 12f) and the boundary layer turbulent
661 kinetic energy is large (not shown), implying that the areas under the wave crests are regions of
662 strong vertical diffusion and weak down-barrier transport of dust, explaining why the isopleths of
663 high dust concentrations (e.g., $> 0.2 \text{ mg m}^{-3}$) increase with barrier distance.

664 A map of the horizontal structure of dust mass path, which is the vertically integrated concentra-
665 tion, also for 23:30 UTC on this date (Fig. 15b) shows coherent northwest-southeast oriented wave
666 fronts of high and low dust mass path that closely follow the orientation of the upwind topography.
667 As such, in addition to depth of the dust layer, trapped waves have a strong effect on the horizontal
668 distribution of dust concentration. A map of the corresponding surface dust emission flux (Fig.
669 15c) does not clearly show any resemblance to the structure of the waves, owing to the dominant
670 influence of surface characteristics on dust emission, suggesting that the spatial structures of dust
671 concentration and mass path are largely the result of advection and diffusion rather than the spatial
672 pattern of emission. We also note that under the wave crests the cross-barrier wind speeds are weak

673 but the along-barrier wind speeds are northerly (not shown), raising the possibility of meridional
674 dust advection there.

675 We again note that while these WRF-Chem simulations are useful in terms of elucidating the
676 general characteristics of dust storms generated by trapped waves, they are of limited use in terms
677 of understanding the specific distribution of dust in the region during these events. Eyewitness
678 accounts and GOES-R and Roundshot camera animations (M1–M3 in the Supplement) show that



649 FIG. 15. Dust simulated by WRF-Chem at 23:30 UTC on March 15, 2021. In 15a are isentropic surfaces at 1
650 C intervals (contours) and dust concentration (mg m^{-3}) along the 33.25°N a zonal transect, in km downwind of
651 the barrier crest. In 15b is the horizontal distribution of dust mass path (g m^{-2}) along the transect in 15a but in
652 zonal units of $^\circ\text{E}$. Black contour lines indicate topography intervals of 250 m, the thick black line indicates the
653 Salton Sea shoreline, and the white horizontal line the latitude of the transect in 15a. The description for 15c is
654 the same as for 15b except that average dust emission over the preceding 30 min ($\text{g m}^{-2} \text{s}^{-1}$) is shown.

679 during these events dust is mainly emitted from the low-lying desert regions (i.e., barrier distances
680 greater than 40 km in Fig. 15a) whereas the model shows little to no emission in this area (Fig. 15c,
681 -116.2 to -116°E and 33.2 to 33.3°N). Ongoing work suggests that apparent unrealistic distribution
682 of dust emission is at least in part due to erroneous land surface type classification.

683 Lastly, our results imply that a third characteristic of dust storms generated by trapped waves
684 is that wave-forced wind speed perturbations, and thus dust emission, can occur far downwind
685 of the barrier. Output from the WRF simulations indicate that surface wind speed perturbations
686 associated with trapped waves occur as far as 100 km downwind of the barrier (Figs. 11, 12).
687 Radiosondes also indicate the presence of waves downwind of the field site during all three cases
688 (Fig. 9), where plots of balloon height and ascent rate as a function of zonal distance from the field
689 site imply that waves are found at barrier distances greater than 100 km (e.g., Figs S6, S8, S13).

690 Wave-forced wind speed perturbations are also likely to have a large impact on dust emission
691 given the power law relation between emission and surface wind speed (e.g., Kok et al. 2014). For
692 example, we consider two idealized cases of downslope windstorms, in which the surface wind
693 speed of the first is constant with barrier distance $u_1(x) = c_1$, and the surface wind speed of the
694 second is sinusoidal about the same mean $u_2(x) = c_1 + c_2 \cos(x)$, a simplification of wind speed
695 perturbations due to the influence of overlying trapped waves. Evoking the dust uplift potential
696 approximation to the relationship between emission and surface wind speed (Marshall et al. 2011)
697 and assuming wind speeds of sufficient magnitude to loft dust, in either case the total dust emission
698 E over a non-dimensionalized distance 2π is

$$E \propto \int_0^{2\pi} u(x)^3$$

699 so that the total emission for the second case E_2 can be expressed as a function of the first case E_1 ,

$$E_2 = E_1 + 3\pi c_1 c_2^2$$

700 where it is implied that the second term is multiplied by some positive constant of proportionality.
701 Thus, there is a larger net flux of dust into the atmosphere for the second case, and this relative
702 increase in emission is proportional to the product of the mean wind speed c_1 and the square of
703 magnitude of the perturbations c_2 .

704 5. Conclusion

705 Observations of three dust outbreaks that occurred in the northwestern Sonoran Desert indicated
706 that these storms were all associated with the presence of trapped lee waves generated by a north-
707 south oriented mountain range. Reanalysis demonstrated that for each case cross-barrier flow was
708 directed over the region by way of a synoptic scale low pressure trough transitioning through the
709 area (Fig. 3). Surface meteorological measurements showed that during trough passage flow over a
710 field site located near the western shoreline of the Salton Sea (Fig. 1) was westerly with wind speeds
711 and gusts exceeding 10 and 20 m s⁻¹, respectively (Fig. 5). Measurements of PM₁₀ (Fig. 6) and
712 animations from a Roundshot camera and GOES-17 (Supplemental Materials M1–M3) indicated
713 the presence of dust across the region, and aerosol optical depth retrievals from a sun photometer
714 and a ceilometer exhibited values greater than 0.3 during the dust outbreaks. Backscatter profiles
715 from the ceilometer suggested that the depths of the dust layers ranged from 700 m to 2 km (Fig.
716 8). Radiosondes released prior to and during the dust events suggested that the high winds were
717 associated with a shallow convective boundary layer, one factor in generating the shallow dust
718 layers, and the presence of a jet in the lower 1.5 km of the atmosphere (Fig. 9). Radiosonde ascent
719 rates implied the presence of trapped waves in the environment downwind of the field site (Figs.
720 9, S6, S8, S10–S13), consistent with numerical simulations conducted with the WRF model
721 showing that each of the dust-producing high wind events were at some point associated with the
722 presence of trapped lee waves (Fig. 11), resulting in positive surface wind speed perturbations far
723 downwind of the wave-generating barrier (Fig. 12).

724 We highlighted several meteorological aspects of the observed and simulated trapped waves that
725 are relevant to understanding the characteristics of the concurrent dust outbreaks. These include
726 the presence of a low level jet whose depth and speed is affected by wave phase and vertical
727 structure, dust layer depths and concentrations that are also dependent upon these factors, and
728 high wind speeds and dust emission more than 100 km downwind the wave source. Output from
729 WRF-Chem provided corroborating evidence that the depth of the dust layer is strongly tied to
730 wave phase, with the model showing the highest dust concentrations under the wave crests. Direct
731 observational evidence to evaluate many aspects of the wave-forced dust storm characteristics (e.g.,
732 the relationship between wave phase and depth of the dust layer) would require measurements of

733 aerosols and meteorology at different wave phases and at concurrent times, something that is not
734 currently possible given the available instrumentation at this single field site.

735 Inversions upwind and near the heights of the ridge of the Peninsular Mountains were noted for
736 the March 15 2021 and February 15 2022 cases (Fig. 10), as well as in the cases examined in Evan
737 et al. (2022c) and Evan (2019). As such, trapped waves are likely a common feature of strong cross
738 barrier flow and dust outbreaks in the region. Observations and modeling from the Owen's
739 valley suggest, however, that the Salton Sea is not unique in this regard (e.g., Grubišić and Billings
740 2007). More work to evaluate the role of trapped waves on dust emission in other dust-emitting
741 regions is warranted, especially since climate models do not directly simulate nor parameterize
742 trapped waves.

743 The Salton Sea is rapidly drying, and thus the area of exposed playa and potential for increasing
744 dust emission is growing. The Salton Sea sits immediately downwind of the field site, and as
745 such trapped waves have the ability to generate high wind speeds and dust over the growing
746 playa surfaces. It is not clear how the drying of the sea and the resultant changes in the surface
747 temperature and sensible and latent heat fluxes will feedback onto wave activity. It is possible that
748 a warming surface will heat the overlying atmosphere resulting in a reduction of wave amplitude
749 (Jiang et al. 2006), although this effect could also increase the strength of the surface winds by
750 allowing isentropes at the barrier level to more frequently reach the downwind surface. It is also
751 unknown how drying of the sea may affect the depth of the dust layer; while increased surface
752 heating implies a deeper convective boundary layer, the interaction of surface warming with wave
753 activity may increase the near surface stability. It is also plausible that radiative heating by the
754 dust will in-turn feedback onto the wave characteristics. Given the rapid environmental change
755 occurring in this region and the health impacts of exposure to dust on the community (Frie et al.
756 2017, 2019; Jones and Fleck 2020; Biddle et al. 2022), more work to elucidate the impacts of the
757 drying Salton Sea on the region's meteorology and air quality is warranted.

758 *Acknowledgments.* Funding for this work was provided by NSF Award AGS-1833173. We thank
759 Trinity Robinson and Tyler Barbero for their assistance on this project, and three anonymous
760 reviewers for their comments on a previous version of this manuscript.

761 *Data availability statement.* Salton Sea AERONET data is available via aeronet.gsfc.nasa.gov/,
762 surface synoptic station data is at mesowest.utah.edu/, GOES-17 satellite data is at
763 www.avl.class.noaa.gov, NEXRAD data is at mesonet.agron.iastate.edu, surface PM₁₀
764 measurements are from www.arb.ca.gov/aqmis2/aqdselect.php, NARR output is avail-
765 able from psl.noaa.gov, and GFS analysis is available from [www.nco.ncep.noaa.gov/pmb/
766 products/gfs/](http://www.nco.ncep.noaa.gov/pmb/products/gfs/). The soundings, surface meteorological data, and CL51 backscatter and extinc-
767 tion profiles used in this manuscript are permanently archived at [https://doi.org/10.6075/
768 J0BV7GTC](https://doi.org/10.6075/10.6075/J0BV7GTC) (Evan et al. 2022b).

769 **References**

770 Biddle, T., R. Chakraborty, Q. Li, M. Maltz, J. Gerrard, D. Lo, and Coauthors, 2022: The drying
771 salton sea and asthma: A perspective on a "natural" disaster. *California Agriculture*,
772 **76 (1)**, 27–36, <https://doi.org/10.3733/ca.2022a0003>.

773 Biddle, T. A., and Coauthors, 2021: Salton sea aerosol exposure in mice induces a pulmonary
774 response distinct from allergic inflammation. *Science of The Total Environment*, 148450,
775 <https://doi.org/10.1016/j.scitotenv.2021.148450>.

776 Buck, B. J., J. King, and V. Etyemezian, 2011: Effects of salt mineralogy on dust emissions, salton
777 sea, california. *Soil Science Society of America Journal*, **75 (5)**, 1971–1985, [https://doi.org/
778 10.2136/sssaj2011.0049](https://doi.org/10.2136/sssaj2011.0049).

779 Burr, A. C., and Coauthors, 2021: Lung inflammatory response to environmental dust exposure in
780 mice suggests a link to regional respiratory disease risk. *Journal of Inflammation Research*, **14**,
781 4035, <https://doi.org/10.2147/JIR.S320096>.

782 Chen, and J. Dudhia, 2001: Coupling an advanced land surface–hydrology model with
783 the penn state–ncar mm5 modeling system. part i: Model implementation and sensitiv-
784 ity. *Monthly Weather Review*, **129 (4)**, 569–585, [https://doi.org/10.1175/1520-0493\(2001\)
785 129<0569:CAALSH>2.0.CO;2](https://doi.org/10.1175/1520-0493(2001)129<0569:CAALSH>2.0.CO;2).

- 786 Chen, S.-H., and W.-Y. Sun, 2002: A one-dimensional time dependent cloud model. *Journal of the*
787 *Meteorological Society of Japan*, **80** (1), 99–118, <https://doi.org/10.2151/jmsj.80.99>.
- 788 Chin, M., R. B. Rood, S.-J. Lin, J.-F. Müller, and A. M. Thompson, 2000: Atmospheric sulfur
789 cycle simulated in the global model gocart: Model description and global properties. *Journal*
790 *of Geophysical Research: Atmospheres*, **105** (D20), 24 671–24 687, [https://doi.org/10.1029/](https://doi.org/10.1029/2000JD900385)
791 2000JD900385.
- 792 Choobari, O. A., P. Zawar-Reza, and A. Sturman, 2014: The global distribution of mineral
793 dust and its impacts on the climate system: A review. *Atmospheric Research*, **138**, 152–165,
794 <https://doi.org/10.1016/j.atmosres.2013.11.007>.
- 795 De Wekker, S. F., and S. D. Mayor, 2009: Observations of atmospheric structure and dy-
796 namics in the owens valley of california with a ground-based, eye-safe, scanning aerosol
797 lidar. *Journal of applied meteorology and climatology*, **48** (7), 1483–1499, [https://doi.org/](https://doi.org/10.1175/2009JAMC2034.1)
798 10.1175/2009JAMC2034.1.
- 799 Doyle, J. D., and D. R. Durran, 2002: The dynamics of mountain-wave-induced rotors. *Journal of*
800 *the Atmospheric Sciences*, **59** (2), 186–201, [https://doi.org/10.1175/1520-0469\(2002\)059<0186:](https://doi.org/10.1175/1520-0469(2002)059<0186:TDOMWI>2.0.CO;2)
801 TDOMWI>2.0.CO;2.
- 802 Durran, D. R., 1986: Another look at downslope windstorms. part i: The development of analogs
803 to supercritical flow in an infinitely deep, continuously stratified fluid. *Journal of Atmospheric*
804 *Sciences*, **43** (21), 2527–2543, [https://doi.org/10.1175/1520-0469\(1986\)043<2527:ALADWP>](https://doi.org/10.1175/1520-0469(1986)043<2527:ALADWP>2.0.CO;2)
805 2.0.CO;2.
- 806 Durran, D. R., 1990: Mountain waves and downslope winds. *Atmospheric processes over complex*
807 *terrain*, Springer, 59–81, https://doi.org/10.1007/978-1-935704-25-6_4.
- 808 Durran, D. R., 2003: Lee waves and mountain waves. *Encyclopedia of atmospheric sciences*, **1161**,
809 1169.
- 810 Evan, A., B. Walkowiak, and R. Frouin, 2022a: On the misclassification of dust as cloud at an
811 aeronet site in the sonoran desert. *Journal of Atmospheric and Oceanic Technology*, **39** (2),
812 181–191, <https://doi.org/10.1175/JTECH-D-21-0114.1>.

- 813 Evan, A. T., 2019: Downslope winds and dust storms in the salton basin. *Monthly Weather Review*,
814 **147 (7)**, 2387–2402, <https://doi.org/10.1175/MWR-D-18-0357.1>.
- 815 Evan, A. T., C. Flamant, M. Gaetani, and F. Guichard, 2016: The past, present and future of african
816 dust. *Nature*, **531 (7595)**, 493–495, <https://doi.org/10.1038/nature17149>.
- 817 Evan, A. T., R. Frouin, A. Kuwano, T. W. Barbero, T. Robinson, and S. R. Wynn, 2022b: Data
818 from: The characteristics of dust storms generated by trapped waves in the lee of mountains.
819 <https://doi.org/10.6075/J0BV7GTC>.
- 820 Evan, A. T., W. Porter, R. Clemesha, A. Kuwano, and R. Frouin, 2022c: Measurements of a dusty
821 density current in the western sonoran desert. *Journal of Geophysical Research: Atmospheres*,
822 e2021JD035830, <https://doi.org/10.1029/2021JD035830>.
- 823 Fast, J. D., W. I. Gustafson Jr, R. C. Easter, R. A. Zaveri, J. C. Barnard, E. G. Chapman, G. A. Grell,
824 and S. E. Peckham, 2006: Evolution of ozone, particulates, and aerosol direct radiative forcing
825 in the vicinity of houston using a fully coupled meteorology-chemistry-aerosol model. *Journal*
826 *of Geophysical Research: Atmospheres*, **111 (D21)**, <https://doi.org/10.1029/2005JD006721>.
- 827 Fernald, F. G., 1984: Analysis of atmospheric lidar observations: some comments. *Applied Optics*,
828 **23 (5)**, 652–653, <https://doi.org/10.1364/AO.23.000652>.
- 829 Field, J. P., and Coauthors, 2010: The ecology of dust. *Frontiers in Ecology and the Environment*,
830 **8 (8)**, 423–430, <https://doi.org/10.1890/090050>.
- 831 Frie, A. L., J. H. Dingle, S. C. Ying, and R. Bahreini, 2017: The effect of a receding saline lake (the
832 salton sea) on airborne particulate matter composition. *Environmental Science & Technology*,
833 **51 (15)**, 8283–8292, <https://doi.org/10.1021/acs.est.7b01773>.
- 834 Frie, A. L., and Coauthors, 2019: Dust sources in the salton sea basin: a clear case of an
835 anthropogenically impacted dust budget. *Environmental Science & Technology*, **53 (16)**, 9378–
836 9388, <https://doi.org/10.1021/acs.est.9b02137>.
- 837 Giles, D. M., and Coauthors, 2019: Advancements in the aerosol robotic network (aeronet) version
838 3 database–automated near-real-time quality control algorithm with improved cloud screen-
839 ing for sun photometer aerosol optical depth (aod) measurements. *Atmospheric Measurement*
840 *Techniques*, **12 (1)**, 169–209, <https://doi.org/10.5194/amt-12-169-2019>.

- 841 Giles, J., 2005: Climate science: The dustiest place on earth. *Nature*, **434 (7035)**, 816–820,
842 <https://doi.org/10.1038/434816a>.
- 843 Ginoux, P., M. Chin, I. Tegen, J. M. Prospero, B. Holben, O. Dubovik, and S.-J. Lin, 2001: Sources
844 and distributions of dust aerosols simulated with the gocart model. *Journal of Geophysical*
845 *Research: Atmospheres*, **106 (D17)**, 20 255–20 273, <https://doi.org/10.1029/2000JD000053>.
- 846 Ginoux, P., J. M. Prospero, T. E. Gill, N. C. Hsu, and M. Zhao, 2012: Global-scale attribution
847 of anthropogenic and natural dust sources and their emission rates based on modis deep blue
848 aerosol products. *Reviews of Geophysics*, **50 (3)**, <https://doi.org/10.1029/2012RG000388>.
- 849 Gläser, G., P. Knippertz, and B. Heinold, 2012: Orographic effects and evaporative cooling along
850 a subtropical cold front: The case of the spectacular saharan dust outbreak of march 2004.
851 *Monthly Weather Review*, **140 (8)**, 2520–2533, <https://doi.org/10.1175/MWR-D-11-00315.1>.
- 852 Grell, G. A., 1993: Prognostic evaluation of assumptions used by cumulus parameterizations.
853 *Monthly weather review*, **121 (3)**, 764–787, [https://doi.org/10.1175/1520-0493\(1993\)121<0764:
854 PEOAUB>2.0.CO;2](https://doi.org/10.1175/1520-0493(1993)121<0764:PEOAUB>2.0.CO;2).
- 855 Grell, G. A., and D. Dévényi, 2002: A generalized approach to parameterizing convection com-
856 bining ensemble and data assimilation techniques. *Geophysical Research Letters*, **29 (14)**, 38–1,
857 <https://doi.org/10.1029/2002GL015311>.
- 858 Grell, G. A., S. E. Peckham, R. Schmitz, S. A. McKeen, G. Frost, W. C. Skamarock, and B. Eder,
859 2005: Fully coupled online chemistry within the wrf model. *Atmospheric Environment*,
860 **39 (37)**, 6957–6975, <https://doi.org/10.1016/j.atmosenv.2005.04.027>.
- 861 Grubišić, V., and B. J. Billings, 2007: The intense lee-wave rotor event of sierra rotors iop 8. *Journal*
862 *of the atmospheric sciences*, **64 (12)**, 4178–4201, <https://doi.org/10.1175/2006JAS2008.1>.
- 863 Grubišić, V., and Coauthors, 2008: The terrain-induced rotor experiment: A field campaign
864 overview including observational highlights. *Bulletin of the American Meteorological Society*,
865 **89 (10)**, 1513–1534, <https://doi.org/10.1175/2008BAMS2487.1>.
- 866 Holben, B. N., and Coauthors, 1998: Aeronet—a federated instrument network and data archive for
867 aerosol characterizatio. *Remote Sensing of Environment*, **66 (1)**, 1–16, [https://doi.org/10.1016/
868 S0034-4257\(98\)00031-5](https://doi.org/10.1016/S0034-4257(98)00031-5).

- 869 Horel, J., and Coauthors, 2002: Mesowest: Cooperative mesonets in the western united states.
870 *Bulletin of the American Meteorological Society*, **83 (2)**, 211–225, [https://doi.org/10.1175/](https://doi.org/10.1175/1520-0477(2002)083<0211:MCMITW>2.3.CO;2)
871 1520-0477(2002)083<0211:MCMITW>2.3.CO;2.
- 872 Huneus, N., and Coauthors, 2011: Global dust model intercomparison in aerocom phase i. *Atmo-*
873 *spheric Chemistry and Physics*, **11 (15)**, 7781–7816, <https://doi.org/10.5194/acp-11-7781-2011>.
- 874 Iacono, M. J., J. S. Delamere, E. J. Mlawer, M. W. Shephard, S. A. Clough, and W. D. Collins, 2008:
875 Radiative forcing by long-lived greenhouse gases: Calculations with the aer radiative transfer
876 models. *Journal of Geophysical Research*, **113 (D13)**, <https://doi.org/10.1029/2008JD009944>.
- 877 IID, I. I. D., 2016: Salton sea air quality mitigation program. Tech. rep., Tech. Rep., Salton Sea
878 Air Quality Team, 281 pp.
- 879 Janić, Z. I., 2001: *Nonsingular implementation of the Mellor-Yamada level 2.5 scheme in the*
880 *NCEP Meso model*. US Department of Commerce, National Oceanic and Atmospheric Admin-
881 istration.
- 882 Janjić, Z. I., 1994: The step-mountain eta coordinate model: Further developments of the con-
883 vection, viscous sublayer, and turbulence closure schemes. *Monthly weather review*, **122 (5)**,
884 927–945, [https://doi.org/10.1175/1520-0493\(1994\)122<0927:TSMECM>2.0.CO;2](https://doi.org/10.1175/1520-0493(1994)122<0927:TSMECM>2.0.CO;2).
- 885 Jiang, H., J. T. Farrar, R. C. Beardsley, R. Chen, and C. Chen, 2009: Zonal surface wind jets across
886 the red sea due to mountain gap forcing along both sides of the red sea. *Geophysical Research*
887 *Letters*, **36 (19)**, <https://doi.org/10.1029/2009GL040008>.
- 888 Jiang, Q., J. D. Doyle, and R. B. Smith, 2006: Interaction between trapped waves and boundary
889 layers. *Journal of the atmospheric sciences*, **63 (2)**, 617–633, <https://doi.org/10.1175/JAS3640.1>.
- 890 Jiang, Q., M. Liu, and J. D. Doyle, 2011: Influence of mesoscale dynamics and turbulence on fine
891 dust transport in owens valley. *Journal of Applied Meteorology and Climatology*, **50 (1)**, 20–38,
892 <https://doi.org/10.1175/2010JAMC2522.1>.
- 893 Jin, Y., and Coauthors, 2015: Ceilometer calibration for retrieval of aerosol optical properties.
894 *Journal of Quantitative Spectroscopy and Radiative Transfer*, **153**, 49–56, [https://doi.org/10.](https://doi.org/10.1016/j.jqsrt.2014.10.009)
895 1016/j.jqsrt.2014.10.009.

896 Jones, B. A., and J. Fleck, 2020: Shrinking lakes, air pollution, and human health: Evidence
897 from california's salton sea. *Science of the Total Environment*, **712**, 136490, [https://doi.org/](https://doi.org/10.1016/j.scitotenv.2019.136490)
898 10.1016/j.scitotenv.2019.136490.

899 Karyampudi, V. M., S. E. Koch, C. Chen, J. W. Rottman, and M. L. Kaplan, 1995: The influence
900 of the rocky mountains on the 13–14 april 1986 severe weather outbreak. part ii: Evolution
901 of a prefrontal bore and its role in triggering a squall line. *Monthly Weather Review*, **123** (5),
902 1423–1446, [https://doi.org/10.1175/1520-0493\(1995\)123<1423:TIOTRM>2.0.CO;2](https://doi.org/10.1175/1520-0493(1995)123<1423:TIOTRM>2.0.CO;2).

903 Kim, K.-M., and Coauthors, 2021: Modeling asian dust storms using wrf-chem during the dragon-
904 asia field campaign in april 2012. *Journal of Geophysical Research: Atmospheres*, **126** (18),
905 e2021JD034793, <https://doi.org/https://doi.org/10.1029/2021JD034793>.

906 Knippertz, P., 2014: Meteorological aspects of dust storms. *Mineral Dust*, P. Knippertz, and
907 J. Stuut, Eds., Springer, 121–147, https://doi.org/10.1007/978-94-017-8978-3_6.

908 Knippertz, P., C. Deutscher, K. Kandler, T. Müller, O. Schulz, and L. Schütz, 2007: Dust mobi-
909 lization due to density currents in the atlas region: Observations from the saharan mineral dust
910 experiment 2006 field campaign. *Journal of Geophysical Research*, **112** (D21), [https://doi.org/](https://doi.org/10.1029/2007JD008774)
911 10.1029/2007JD008774.

912 Koch, S. E., P. B. Dorian, R. Ferrare, S. Melfi, W. C. Skillman, and D. Whiteman, 1991: Structure
913 of an internal bore and dissipating gravity current as revealed by raman lidar. *Monthly Weather*
914 *Review*, **119** (4), 857–887, [https://doi.org/10.1175/1520-0493\(1991\)119<0857:SOAIBA>2.0.](https://doi.org/10.1175/1520-0493(1991)119<0857:SOAIBA>2.0.CO;2)
915 CO;2.

916 Kok, J., and Coauthors, 2014: An improved dust emission model—part 1: Model description and
917 comparison against measurements. *Atmospheric Chemistry and Physics*, **14** (23), 13023–13041,
918 <https://doi.org/https://doi.org/10.5194/acp-14-13023-2014>.

919 Kok, J. F., D. S. Ward, N. M. Mahowald, and A. T. Evan, 2018: Global and regional importance of
920 the direct dust-climate feedback. *Nature Communications*, **9** (1), 1–11, [https://doi.org/10.1038/](https://doi.org/10.1038/s41467-017-02620-y)
921 s41467-017-02620-y.

- 922 LeGrand, S. L., C. Polashenski, T. W. Letcher, G. A. Creighton, S. E. Peckham, and J. D. Cetola,
923 2019: The afwa dust emission scheme for the gcart aerosol model in wrf-chem v3. 8.1.
924 *Geoscientific Model Development*, **12** (1), 131–166, <https://doi.org/10.5194/gmd-12-131-2019>.
- 925 Marcos, C. R., J. L. Gómez-Amo, C. Peris, R. Pedrós, M. P. Utrillas, and J. A. Martínez-Lozano,
926 2018: Analysis of four years of ceilometer-derived aerosol backscatter profiles in a coastal site
927 of the western mediterranean. *Atmospheric Research*, **213**, 331–345, [https://doi.org/10.1016/j.](https://doi.org/10.1016/j.atmosres.2018.06.016)
928 [atmosres.2018.06.016](https://doi.org/10.1016/j.atmosres.2018.06.016).
- 929 Marsham, J. H., P. Knippertz, N. S. Dixon, D. J. Parker, and G. M. Lister, 2011: The importance of
930 the representation of deep convection for modeled dust-generating winds over west africa during
931 summer. *Geophysical Research Letters*, **38** (16), <https://doi.org/10.1029/2011GL048368>.
- 932 Marticorena, B., and G. Bergametti, 1995: Modeling the atmospheric dust cycle: 1. design of a
933 soil-derived dust emission scheme. *Journal of geophysical research: atmospheres*, **100** (D8),
934 16 415–16 430, <https://doi.org/https://doi.org/10.1029/95JD00690>.
- 935 Mayr, G. J., and L. Armi, 2010: The influence of downstream diurnal heating on the descent of
936 flow across the sierras. *Journal of Applied Meteorology and Climatology*, **49** (9), 1906–1912,
937 <https://doi.org/10.1175/2010JAMC2516.1>.
- 938 Mesinger, F., and Coauthors, 2006: North american regional reanalysis. *Bulletin of the American*
939 *Meteorological Society*, **87** (3), 343–360, <https://doi.org/10.1175/BAMS-87-3-343>.
- 940 Miller, P., M. Williams, and T. Mote, 2021: Modeled atmospheric optical and thermodynamic
941 responses to an exceptional trans-atlantic dust outbreak. *Journal of Geophysical Research:*
942 *Atmospheres*, **126** (5), e2020JD032 909, <https://doi.org/https://doi.org/10.1029/2020JD032909>.
- 943 Monin, A. S., and A. M. Obukhov, 1954: Basic laws of turbulent mixing in the surface layer of the
944 atmosphere. *Contrib. Geophys. Inst. Acad. Sci. USSR*, **151** (163), e187.
- 945 Münkel, C., N. Eresmaa, J. Räsänen, and A. Karppinen, 2007: Retrieval of mixing height
946 and dust concentration with lidar ceilometer. *Boundary-Layer Meteorology*, **124** (1), 117–128,
947 <https://doi.org/10.1007/s10546-006-9103-3>.
- 948 Nappo, C. J., 2013: *An introduction to atmospheric gravity waves*. Academic press.

949 NCEI, ????: U.s. climate normals. URL [https://www.ncei.noaa.gov/products/land-based-station/
950 us-climate-normals.](https://www.ncei.noaa.gov/products/land-based-station/us-climate-normals)

951 NCEP, 2013: Ncep office note 442: The gfs atmospheric model. Washington DC: sn.

952 Parajuli, S. P., and C. S. Zender, 2017: Connecting geomorphology to dust emission through high-
953 resolution mapping of global land cover and sediment supply. *Aeolian Research*, **27**, 47–65,
954 <https://doi.org/https://doi.org/10.1016/j.aeolia.2017.06.002>.

955 Parajuli, S. P., and C. S. Zender, 2018: Projected changes in dust emissions and regional air quality
956 due to the shrinking salton sea. *Aeolian Research*, **33**, 82–92, [https://doi.org/10.1016/j.aeolia.
957 2018.05.004](https://doi.org/10.1016/j.aeolia.2018.05.004).

958 Peckham, S. E., and Coauthors, 1991: Wrf-chem version 3.9.1.1 user's guide. Tech. rep., Na-
959 tional Center for Atmospheric Research. URL [https://ruc.noaa.gov/wrf/wrf-chem/Users_guide.
960 pdf](https://ruc.noaa.gov/wrf/wrf-chem/Users_guide.pdf).

961 Pokharel, A. K., M. L. Kaplan, and S. Fiedler, 2017: Subtropical dust storms and downslope
962 wind events. *Journal of Geophysical Research: Atmospheres*, **122** (19), 10–191, [https://doi.org/
963 10.1002/2017JD026942](https://doi.org/10.1002/2017JD026942).

964 Poudel, U., S. Ahmad, and H. Stephen, 2021: Studying the intra-annual variability in surface
965 area and volume of salton sea, california, using remote sensing-based water indices and gis.
966 *World Environmental and Water Resources Congress 2021*, 769–783, [https://doi.org/10.1061/
967 9780784483466.070](https://doi.org/10.1061/9780784483466.070).

968 Prospero, J. M., P. Ginoux, O. Torres, S. E. Nicholson, and T. E. Gill, 2002: Environmental
969 characterization of global sources of atmospheric soil dust identified with the nimbus 7 total
970 ozone mapping spectrometer (toms) absorbing aerosol product. *Reviews of geophysics*, **40** (1),
971 2–1–2–31, <https://doi.org/10.1029/2000RG000095>.

972 Pu, B., and P. Ginoux, 2018: How reliable are cmip5 models in simulating dust opti-
973 cal depth? *Atmospheric Chemistry and Physics*, **18** (16), 12 491–12 510, [https://doi.org/
974 10.5194/acp-18-12491-2018](https://doi.org/10.5194/acp-18-12491-2018).

- 975 Ralph, F. M., P. J. Neiman, T. L. Keller, D. Levinson, and L. Fedor, 1997: Observations, simulations,
976 and analysis of nonstationary trapped lee waves. *Journal of the atmospheric sciences*, **54** (10),
977 1308–1333, [https://doi.org/10.1175/1520-0469\(1997\)054<1308:OSAAON>2.0.CO;2](https://doi.org/10.1175/1520-0469(1997)054<1308:OSAAON>2.0.CO;2).
- 978 Ryerson, T., and Coauthors, 2013: The 2010 california research at the nexus of air quality and
979 climate change (calnex) field study. *Journal of Geophysical Research: Atmospheres*, **118** (11),
980 5830–5866, <https://doi.org/10.1002/jgrd.50331>.
- 981 Scorer, R. S., 1949: Theory of waves in the lee of mountains. *Quarterly Journal of the Royal*
982 *Meteorological Society*, **75** (323), 41–56, <https://doi.org/10.1002/qj.49707532308>.
- 983 Shao, Y., and Coauthors, 2011: Dust cycle: An emerging core theme in earth system science.
984 *Aeolian Research*, **2** (4), 181–204, <https://doi.org/10.1016/j.aeolia.2011.02.001>.
- 985 Skamarock, W. C., and Coauthors, 2019: A description of the advanced research wrf model version
986 4. *National Center for Atmospheric Research: Boulder, CO, USA*, 145.
- 987 Smith, R. B., 2019: 100 years of progress on mountain meteorology research. *Meteorological*
988 *Monographs*, **59**, 20–1, <https://doi.org/10.1175/AMSMONOGRAPHS-D-18-0022.1>.
- 989 Stephen, M. F., and D. S. Gorsline, 1975: Sedimentary aspects of the new river delta, salton sea,
990 imperial county, california.
- 991 Strauss, L., S. Serafin, and V. Grubišić, 2016: Atmospheric rotors and severe turbulence in a
992 long deep valley. *Journal of the Atmospheric Sciences*, **73** (4), 1481–1506, <https://doi.org/10.1175/JAS-D-15-0192.1>.
- 994 Sweeney, M. R., E. V. McDonald, and V. Etyemezian, 2011: Quantifying dust emissions from
995 desert landforms, eastern mojave desert, usa. *Geomorphology*, **135** (1-2), 21–34, <https://doi.org/10.1016/j.geomorph.2011.07.022>.
- 997 Todd, M. C., R. Washington, S. Raghavan, G. Lizcano, and P. Knippertz, 2008: Regional model
998 simulations of the bodélé low-level jet of northern chad during the bodélé dust experiment (bodex
999 2005). *Journal of Climate*, **21** (5), 995–1012, <https://doi.org/10.1175/2007JCLI1766.1>.

- 1000 Wiegner, M., and Coauthors, 2014: What is the benefit of ceilometers for aerosol remote
1001 sensing? an answer from earlinet. *Atmospheric Measurement Techniques*, **7** (7), 1979–1997,
1002 <https://doi.org/10.5194/amt-7-1979-2014>.
- 1003 Yang, S., J. Preißler, M. Wiegner, S. von Löwis, G. N. Petersen, M. M. Parks, and D. C. Finger,
1004 2020: Monitoring dust events using doppler lidar and ceilometer in iceland. *Atmosphere*, **11** (12),
1005 1294, <https://doi.org/10.3390/atmos11121294>.
- 1006 Yuan, T., S. Chen, J. Huang, X. Zhang, Y. Luo, X. Ma, and G. Zhang, 2019: Sensitivity of
1007 simulating a dust storm over central asia to different dust schemes using the wrf-chem model.
1008 *Atmospheric Environment*, **207**, 16–29, [https://doi.org/https://doi.org/10.1016/j.atmosenv.2019.](https://doi.org/https://doi.org/10.1016/j.atmosenv.2019.03.014)
1009 03.014.
- 1010 Zhao, A., C. L. Ryder, and L. J. Wilcox, 2022: How well do the cmip6 models simulate dust
1011 aerosols? *Atmospheric Chemistry and Physics*, **22** (3), 2095–2119, [https://doi.org/10.5194/](https://doi.org/10.5194/acp-22-2095-2022)
1012 [acp-22-2095-2022](https://doi.org/10.5194/acp-22-2095-2022).
- 1013 Zucca, C., N. Middleton, U. Kang, and H. Liniger, 2021: Shrinking water bodies as hotspots of
1014 sand and dust storms: The role of land degradation and sustainable soil and water management.
1015 *Catena*, **207**, 105 669, <https://doi.org/10.1016/j.catena.2021.105669>.